Fall 2011

Electrical properties of growing porous anodic aluminum oxide films

Joseph L. Iuliucci
University of New Hampshire, Durham

ELECTRICAL PROPERTIES OF GROWING POROUS ANODIC ALUMINUM OXIDE FILMS

BY

Joseph L. Iuliucci

B.Sc., University of New Hampshire, 2007

THESIS

Submitted to The University of New Hampshire

in Partial Fulfillment of

the Requirements for the Degree of

Master of Science

In

Chemical Engineering

September 2011

ProQuest LLC
789 East Eisenhower Parkway
P.O. Box 1346
Ann Arbor, MI 48106-1346

ACKNOWLEDGEMENTS

I would like to acknowledge the support and guidance of my advisor, Dr. Dale Barkey, without which this work would not have been possible. His poise, patience and critical thinking are invaluable characteristics to which I aspire.

To my committee, I cannot thank you enough for the valuable advice during the writing and revision process leading to this completed work.

I would like to express my gratitude to the Department of Chemical Engineering and the University of New Hampshire for this opportunity as well as financial support during the pursuit of this degree. Special thanks to Dr. P.T. Vasudevan for his friendly advice and conversation.

Finally, I would like to thank my family: Robert and Rosalynn Iuliucci, and Elizabeth Hartt; and my partner, Melanie Nelson. The completion of this work and degree is in no small way a testament to your understanding, support, and encouragement. Thank you.

TABLE OF CONTENTS

LIST OF FIGURES

LIST OF TABLES

ABSTRACT

ELECTRICAL PROPERTIES OF GROWING POROUS ANODIC ALUMINUM OXIDE FILMS

by

Joseph L. Iuliucci

University of New Hampshire, September, 2011

Electrochemical oxidation of aluminum and aluminum alloys in acid electrolytes results in a coating with ordered structure on the nano-scale. Although this highly functional nano-material is available commercially for a diverse range of applications, the driving forces responsible for structure development are not well understood. Two electrical properties, the resistance and capacitance, contain information about the current, space charge and electric field distribution during structure development. The electrical properties of porous oxide films were extracted *in situ* during growth on three base materials at varying temperatures and current densities. In this work, a single frequency electrochemical impedance spectroscopy technique and an experimental apparatus designed for *in situ* measurement of cell potential and current were used. The electrical properties calculated during structure development in sulfuric acid at current densities between 5 and 35 $mA \cdot cm^{-2}$ support the hypothesis that structure originates from competition between electrostatic forces and viscous dissipation.

CHAPTER 1

INTRODUCTION

Electrochemical oxidation, also known as anodizing, imparts an integral corrosion and abrasion resistant coating on industrially important metals. Aluminum and aluminum alloys have been treated using anodizing for nearly a century. These metals react spontaneously with ambient oxygen to form a thin oxide coating. Unlike other metal oxides, aluminum oxide does not flake; the oxide adheres to the metal preventing further oxidation. To exploit the corrosion and abrasion protection provided by aluminum oxide, forced thickening of the coating is accomplished electrochemically.

The coating can be thickened by imposing an anodic current or positive potential on the metal/oxide interface, driving the formation of aluminum oxide. Aluminum oxide (alumina) is formed as metal is consumed by oxidation at the anode of an electrochemical cell. Oxidized metal ions react with oxygen to form oxide, Al_2O_3. When this forced thickening is performed in certain high conductivity electrolytes the resulting oxide film has interesting and useful structure on the nano-scale. The film structure, displayed in figure 1.1, is characterized by an ordered array of hexagonal cells, each containing a roughly centered pore. Due to the high order and small scale the films are commercially available as filters, nano-wire and nano-tube templates, and scaffolds for biomedical applications including tissue engineering. Commercial films are available in a relatively narrow range of structural dimensions. The range of morphology is limited by the

necessity to tailor the films using process refinement. Although correlations link the film dimensions to anodizing conditions they provide merely a starting point for commercial processes. To fully exploit the incredible functionality of ordered nano porous aluminum oxide films a growth model must be developed. To date there is no unified mechanism that satisfactorily explains the multiple stages of growth observed during porous oxide growth.

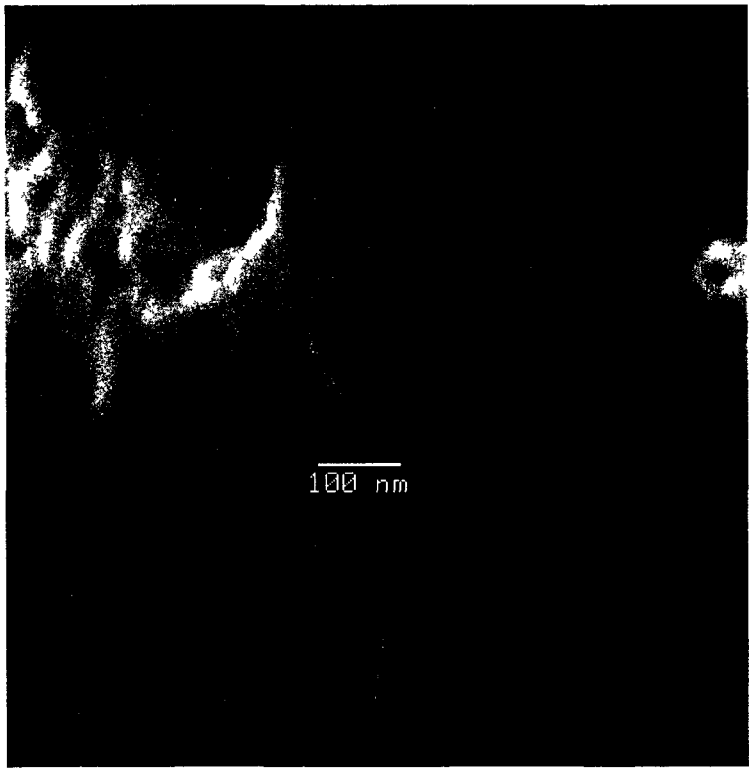

Figure 1.1: SEM image indicating ordered hexagonal cells with a 100 nm pore spacing and 20 nm pore diameter.

In order to further a unified growth mechanism it is necessary to probe the driving forces that lead to nano-structure development. Although it has been alternatively hypothesized that enhanced chemical dissolution is the origin of ordered structure in aluminum oxide films, the ordered nano-scale structure observed in anodic aluminum oxide formed in sulfuric acid at current densities between 5 and 35 $mA \cdot cm^{-2}$ primarily

originates from competition between electrostatic forces and viscous dissipation by oxide flow in the barrier layer at pore bases.

1.1 Objectives

To date there is no theory of growth capably describing the multiple stage film-formation observed during porous aluminum oxide production. To better understand the driving forces leading to the nano-scale ordered structure of porous films an *in situ* technique was proposed and implemented. The novel application of this existing technique makes it possible to calculate two electrical properties during growth of porous films. These electrical properties, the resistance and capacitance, were identified as describing the current, space charge and electric field distribution during structure development and steady growth[1]. Electrochemically produced aluminum oxide films develop structure that is characterized by an array of hexagonal cells each containing a roughly centered pore that extends perpendicularly from the oxide surface to a thin continuous film overlaying the metal. Sulfuric and other acid baths have been shown to be effective in the production of thick porous oxide films structured on the scale of tens to hundreds of nanometers. Electrochemically produced films with ordered structure are available as a commercial nano-material. These films are applied as electrolytic capacitors, filters, templates for nano-tube and nano-wire production and decorative coatings. However, the range of dimensions of commercially available films is narrow because the mechanism leading to long range patterning of these films is not as yet well understood. To exploit the functionality of this nano-material it is desired to develop a model capable of describing the development and ordering of structure. A model requires clear understanding of the driving forces leading to structure development

It has been variously proposed that thermal or field enhanced dissolution of oxide; stresses in the film due to volume constraints and charge attraction, and oxide flow are factors in the morphological development of anodic aluminum oxide (AAO) films. No unified model accounts for the experimental observations of staged growth and ordered films. The present work is guided by the hypothesis that porous growth proceeds by electrostriction induced flow instability and dynamic re-stabilization by viscous forces[2]. The basis of this hypothesis is the high driving force associated with oxidation of aluminum and experimental evidence of flow in the thin continuous layer that is inconsistent with a dissolution model. The application of an *in situ* single frequency electrochemical technique capable of extracting the electrical properties of the film during onset of growth, development of instability, and re-stabilization with porous morphology has been proposed as a method of elucidating the growth processes of porous AAO[1].

1.2 The Electrochemistry of Anodizing

1.2.1 The Electrochemical Cell

Anodizing is performed experimentally and industrially in an electrochemical cell. An electrochemical cell is a circuit containing two electrodes separated by a conducting electrolyte phase. In a two electrode system there is an anode and a cathode. At the anode material is stripped of electrons and oxidized. At the cathode electrons are available at the electrode/solution interface and species are reduced. The two electrodes are directly wired outside the cell or connected via instrumentation. In the wet cell the circuit is completed by the conducting electrolyte. A schematic representation of an electrochemical cell is presented in figure 1.2. During anodizing the working metal

sample is the anode and the cathode can be any material that is unreactive in the chosen electrolyte.

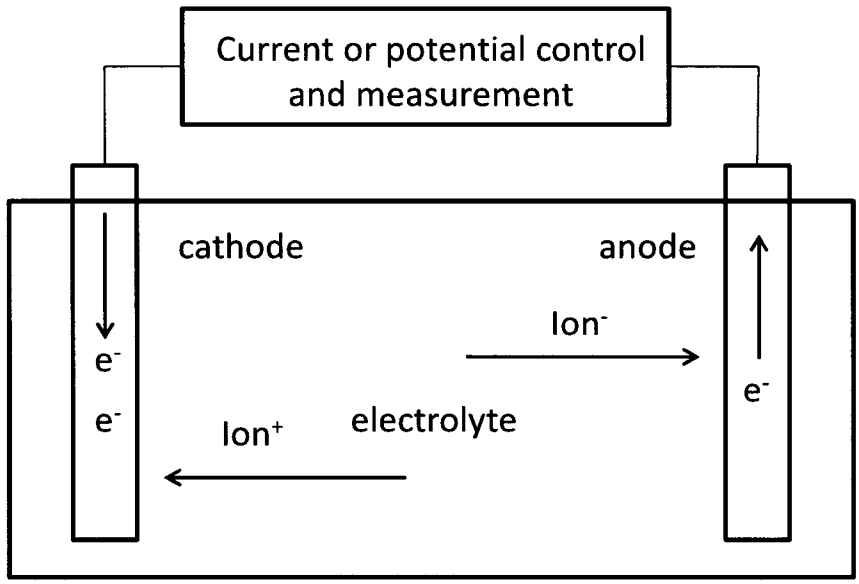

Figure 1.2: Schematic representation of an electrochemical cell with electrode connected through a measurement/control instrument.

Two types of processes occur at the electrodes in electrochemical cells: faradaic and nonfaradaic. A faradaic process entails transfer of charge across the electrode/solution interface. For this type of process the extent of chemical reaction caused by flowing current is related to the amount of charge passed. The Faraday constant, F, is the amount of charge on one mole of electrons, equal to 96,485 coulombs per mole ($C \cdot mol^{-1}$); thus reactants and products of electrochemical reactions are related to the current by this constant. In processes such as acid anodizing, competing reactions make the overall reaction less than 100 % efficient. Moreover, in porous oxide growth a portion of oxidized aluminum is ejected directly into the electrolyte. The loss of metal ions means the mass of oxide produced cannot be directly predicted from the faradaic current. Studies suggest the faradaic efficiency is in the range of 30-80 % for porous oxide formation and increases with applied current or potential[3].

Nonfaradaic processes include adsorption, desorption and double layer charging. In figure 1.3 a planar electrode interface indicates the difference between the two processes. The double layer becomes charged when surface charges spanning the electrode interface attract free ions in solution. In figure 1.3 negative ions are adsorbed, spanning the interface with a negative charge, and positive free ions in the bulk are attracted to the charge layer. Nonfaradaic phenomena actively alter the electrode solution interface and result in external transient currents but do not cause charge to cross the electrode interface.

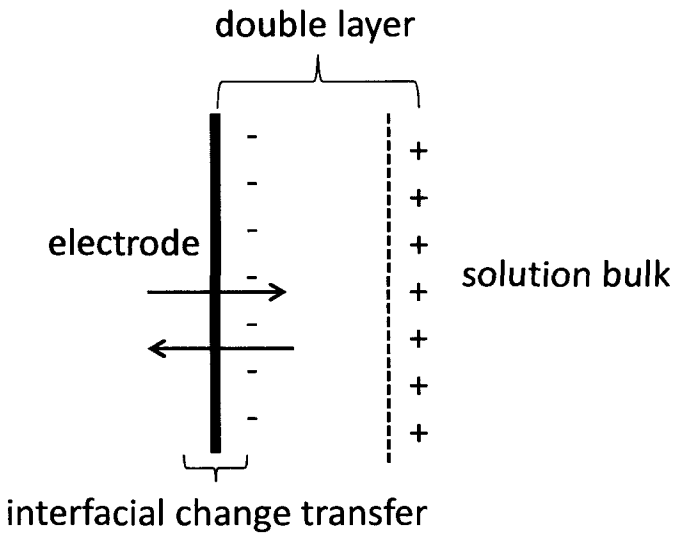

Figure 1.3: A planar electrode interface indicating faradaic and nonfaradaic electrode processes.

1.2.3 Electrochemical Oxidation

Electrochemical oxidation or anodizing is an electrochemical process used to thicken a naturally occurring oxide layer on aluminum, aluminum alloys and other industrially important metals. As the name suggests, the process involves passing an anodic current or imposing a positive potential on the metal/solution interface. The process oxidizes metal to metal ion which in turn reacts with water in the bath solution to

form the oxide coating. In general the electrochemical reaction forming aluminum oxide on pure aluminum and aluminum alloys proceeds as

$$2Al + 3H_2O \rightarrow Al_2O_3 + 3H_2 \quad (1.1)$$

Although this adequately describes the overall cell reaction during aluminum anodizing it offers no insight into the complex system of reactions taking place at multiple reaction interfaces.

Anodizing has been employed industrially to increase the corrosion and wear resistance of aluminum and aluminum alloys for nearly a century. Several types of oxide coatings can be produced depending on bath chemistry, temperature, and anodizing method. This study is focused only on the general distinction between barrier type (non-porous) and porous oxide films. Barrier films are frequently formed in alkaline electrolytes. The films are thin relative to porous films but have better mechanical properties because they do not have the void space of pores. Porous films can be described as a composite film. They contain a thin continuous non-porous film immediately overlaying the metal; this is named the barrier layer. The porous layer extends from the barrier layer to the surface of the film. During steady growth of porous films the porous layer thickens while the barrier layer remains a constant thickness. It is possible to grow very thick porous oxide films, on the order of several microns.

In early AAO research it was noted that films formed on aluminum and aluminum alloys in acid baths were comparatively soft but little other than this macroscopic observation distinguished the films. The films are comparatively soft due to the void space of the pores. Originally it was important to avoid the soft coatings formed in acid baths as anodizing was primarily used to bolster the mechanical properties of the metal.

With the evolution of analytical science, a picture of porous oxide emerged. The films are characterized by regular structure on the nanometer scale. Many early manuscripts investigate porous films as pure science, pushing towards a unified theory of growth. Exhaustive experimental work correlated dimensional characteristics of the film with temperature, bath chemistry and formation potential. In 1995 Masuda et al. demonstrated the production of highly ordered films and their functionalization as nano-wire templates[4,5]. Porous alumina films immediately became a commercial technology and an intense area of research.

1.2.3 Oxidation of Aluminum

The process of oxidation occurs at ambient conditions for many metals. Aluminum and aluminum alloys spontaneously react with ambient oxygen to produce an oxide layer with a thickness of 2-7 nm. On some metals, like iron, oxide is undesirable as it has the tendency to flake. On aluminum, the oxide adheres to the metal and protects against further corrosion. To exploit the properties of oxide it is desirable to thicken the naturally formed coating. In figure 1.4 the oxide layer is shown overlaying the metal.

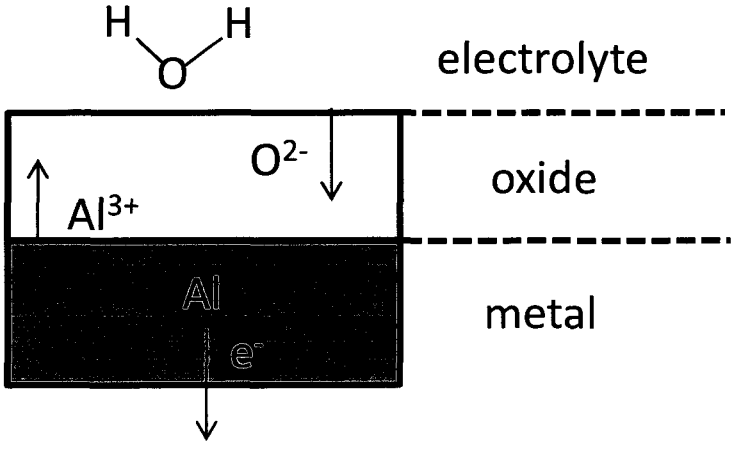

Figure 1.4: Oxidation of metal and reaction with oxygen in water to form oxide coating.

In order to thicken the oxide layer, the reactants, oxygen and aluminum, must be brought to a reaction plane. In aluminum oxide formation it is a large magnitude electric field that drives ions across the film. To establish the electric field, either a potential or a current is imposed on the metal interface. Potentiostatic anodizing requires a postive potential in the range of 10 V to more than 200 V depending on cell conditions. Alternatively, as in this study, galvanic control can be implemented. Galvanically produced films result from controlling the anodic current across the metal/oxide interface. Both potential and galvanic anodizing oxidize the metal to metal ion by stripping electrons from the material

$$Al^{o} \rightarrow Al^{3+} + 3e^{-} \tag{1.2}$$

Electrons flow through the external circuit and are available at the cathode. Hydrogen ions in solution are reduced at the cathode and form hydrogen gas

$$2H^{+}(aq) + 2e^{-} \rightarrow H_2 \tag{1.3}$$

These oxidation-reduction reactions describe the processes at the anode and cathode respectively. The reaction forming aluminum oxide must be regarded while considering multiple reaction planes. There are two reactants in the formation of aluminum oxide, aluminum and oxygen. Aluminum ions originate in the metal where it is oxidized. Oxygen ions are provided by water as it breaks down at or near the oxide/electrolyte interface. In figure 1.4 it can be observed that reaction requires transfer of reactant ions across the formed oxide. The important interfaces in the uniform film are the metal/oxide and oxide/electrolyte interfaces indicated by dashed lines in figure 1.4. At the oxide/electrolyte interface four key reactions take place simultaneously. The previously formed oxide is dissolved by the acid electrolyte

$$Al_2O_3 \rightarrow 2Al^{3+} + 3O^{2-} \tag{1.4}$$

Whether this reaction is accelerated during anodizing and to what extent this reaction influences the formation of porous oxides is a point of contention and will be addressed in a following section. Reactant oxygen is ejected into the oxide as water dissociates at the interface

$$H_2O \leftrightarrow 2H^+(aq) + O^{2-}(ox) \tag{1.5}$$

The oxygen anion is a mobile charge carrier in the film and accounts for 60 % of the ionic current. The other 40 % is carried by metal cations[6]. During porous oxide growth metal cations that reach the oxide/electrolyte interface dissolve into the bath solution

$$Al^{3+}(ox) \rightarrow Al^{3+}(aq) \tag{1.6}$$

by ion transfer[7]. This ejection and loss of metal cations appears during porous oxide growth only. In barrier type films, metal cations at the oxide/electrolyte interface may react directly with water molecules through the following reaction

$$2Al^{3+} + 3H_2O \rightarrow Al_2O_3 + 6H^+ \tag{1.7}$$

During porous growth, new oxide is formed primarily at a reaction plane nearby the metal/oxide interface. The production of oxide material follows

$$2Al^{3+}(ox) + 3O^{2-}(ox) \rightarrow Al_2O_3 \tag{1.8}$$

where oxidized aluminum reacts with inwardly migrating oxygen ions.

1.3 Porous Anodic Coatings

Despite significant research efforts no mechanism yet thoroughly describes porous film growth. However, decades of research provides information regarding the growth behavior and physical dimensions of porous films. The growth proceeds through multiple stages with the basic porous morphology developing early in growth. Once the

structure develops the films are characterized by a soft porous layer overlaying a thin continuous film termed the barrier layer.

The porous oxide is described as a nano-scale ordered array of hexagonal cells. Each cell contains a roughly centered pore that extends perpendicularly from the film surface to the barrier layer. During anodizing these pores are filled with electrolyte making the barrier layer surface at the pore base an oxide/electrolyte interface. An idealized hexagonal cell and pore distribution appear in figure 1.5. The pore walls in the figure are tapered to exaggerate the deviation from an ideal cylindrical pore that appears in thick porous films. The pore diameter, D, can range between 10-400 nm, the spacing, λ, is on the order of 100 nm and the barrier layer thickness is 10's of nanometers thick. The dimensions of the film are significantly influenced by the bath chemistry, temperature, and pre-patterning, and have been correlated with formation potential. Because the films are highly ordered on the nano-scale, they have been researched extensively for filters and technological applications. Commercially available films including those used as filters and templates rely on experimental process refinement to produce a relatively narrow range of film morphologies. A unified theory of the porous AAO growth mechanism is the key to further development of this highly functional nano-structured material. This work strives to elucidate the driving forces behind structure development by evaluating the electrical properties of growing films.

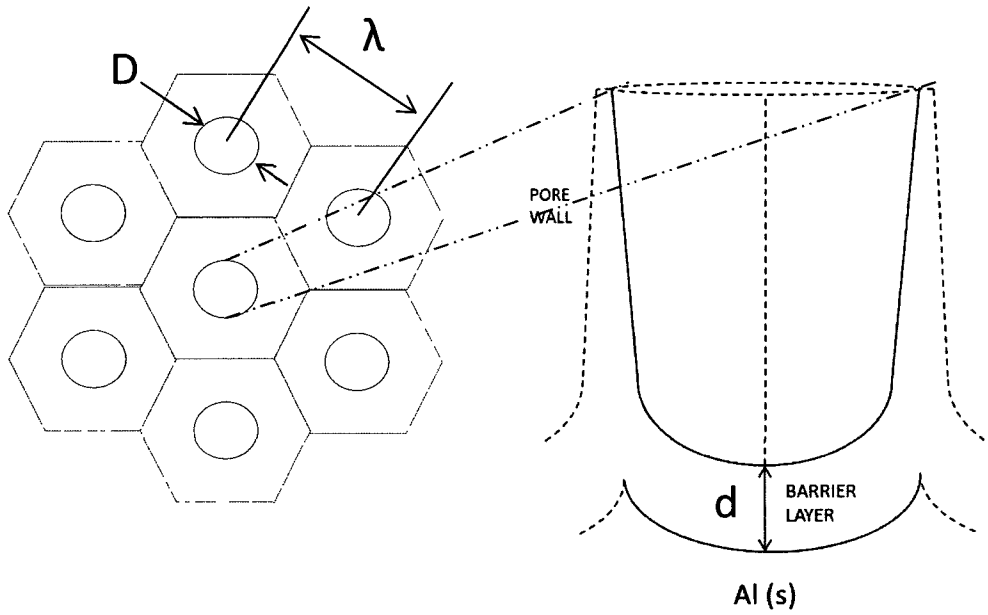

Figure 1.5: Vertical view of hexagonal cell distribution and 2D representation of a single pore including diameter, D, pore spacing, λ, and barrier layer thickness, d.

1.4 Mechanisms of Porous Film Growth

The growth of porous films can be described as proceeding through two general stages. The initial stage, called hereafter the transient stage, involves rapid thickening of a non-porous film followed by pore development. The second stage, called the steady growth stage, is characterized by constant barrier layer thickness and an increasing porous layer thickness. During the growth of porous films there is significant loss of metal ions as they are ejected by ion transfer from the film into the electrolyte at the pore base. By comparison, barrier type films form with oxidized metal loss. Thus, in highly conductive low pH electrolytes, aluminum ions that migrate across the film to the oxide/electrolyte interface do not react with oxygen but are directly ejected into the electrolyte[8-10]. Consequently, during porous oxide growth the metal/oxide interface is treated as the principal reaction plane for oxide production. The identification of the

metal/oxide interface as the region of oxide generation means there is a significant volume source at the base of each pore.

There are few widely accepted components of the AAO growth mechanism. In the course of anodic film research both chemical and mechanical considerations have been scrutinized in an attempt to explain pore initiation, pore ordering and steady growth of porous films with fixed barrier layer thickness. The following are reviews of pertinent mechanisms and a brief presentation of the flow instability hypothesis recently proposed by Barkey and McHugh[2].

1.4.1 Dissolution

Enhanced dissolution has been the single most investigated mechanism of porosity in anodic films. The argument stems from the production of porous films in low pH electrolytes. Acids chemically dissolve oxide films upon immersion but at a nearly negligible rate in comparison to that of oxide generation during anodizing. It was proposed that the dissolution rate be viewed as a locally enhanced phenomenon. A thermally or Joule's effect enhanced mechanism has given way to a field enhanced mechanism[11]. The concept was demonstrated schematically by O'Sullivan and Wood where the oxide was represented as a crude lattice to show how polarization of the Al-O bonds during anodizing make the film more susceptible to dissolution[12]. This model relies on preferential sites of chemical attack. On the scale of several nano-meters the naturally formed oxide layer is non-uniform. These defects result in sites where oxide dissolves and forms a pit site. Applied potential not only increases production of oxide material but also increases the number and size of pits, concentrating the electric field at defect sites[13]. For this dissolution hypothesis to adequately describe the steady stage of

growth the local rate of dissolution and generation must be equal at opposite interfaces at the pore base. There is no evidence that indicates the rate of dissolution is on the same order as the rate of oxide production.

Evidence of enhanced dissolution is speculative at best. Capacitance measurements taken *in situ* during a potential step were suggested as experimental evidence of the dissolution phenomenon[14]. During anodizing, a sudden drop in potential spurs a corresponding drop in anodic current, but this is followed by the re-establishment of the pre-drop current. Early studies did not account for the structural adjustment that accompanies a change in anodizing conditions[15]. Various tracer studies have been performed that indicated dissolution, whether chemical or field-assisted, is not responsible for pore intitiation[10].

One such study used barrier films produced in an O^{18} enriched environment to study pore development. The barrier films were re-anodized in pore forming electrolytes. The tracer oxygen profile at the pore base indicated retention of the marker oxygen. This indicates that the barrier film had not dissolved significantly when pores formed. It was further suggested that to remain consistent with a dissolution model the marker oxygen must be re-incorporated into the film.

The most recent experimental studies endeavor to isolate and identify the role of dissolution[15,3]. Dissolution alone cannot explain the long range structure or material tracer behavior. Oh and Thompson used prepared barrier films to investigate the development of porous morphology. Similar to the marker oxygen studies, pre-formed barrier films were re-anodized in conventional pore forming electrolytes. The electric field strength across the oxide was varied and the resulting structure characterized.

Although dissolution resulted in pores, there existed a distinct transition in morphology when the field was increased. The group identified critical field strength, above which mechanical instability and plastic deformation lead to larger scale patterning[15].

Similarly, a recent study using galvanic anodizing indicates 5 $mA \cdot cm^{-2}$ may signify a transition current density between a chemical and mechanical pore origin[3]. In a comprehensive work by Zhou et al. they demonstrate the variation in volume expansion factor with current density. This measurement is a ratio between the volume of oxide produced and the volume of metal consumed. They suggest pores develop primarily from dissolution at current densities below 5 $mA \cdot cm^{-2}$, while at and above this current density mechanical deformation and flow dominates.

1.4.1.1 Self-Assembly

The porous aluminum oxide films produced in acid electrolytes are described as having highly ordered structure. It has been presented that dissolution results in pitting of the formed oxide. A satisfactory growth mechanism must not only explain the production of pores but also indicate how pit sites evolve into the highly ordered array of cells and pores observed in porous AAO. Various groups identify the self-assembly of pit sites based on formation potential[5,16,17]. Jessensky et al. present the argument that significant mechanical stress in the oxide from the volume expansion of material production is responsible for the self-adjustment of pore spacing[17]. When aluminum at the working electrode is oxidized and reacts with oxygen, it forms a material with a substantially greater molar volume than the base metal. The molar volume of Al_2O_3 is approximately 2.5 times greater than that of the metal. In this model pores initiate at pitting sites by a dissolution mechanism, the production of material is constrained by pits and thus the sites

order. The expansion during oxidation causes a repulsive force between neighboring pores as material is injected to the layer at each pore base and is forced into the pore walls. A volume expansion factor is defined as the ratio of volume of produced oxide to consumed metal. The production of ordered porous films falls into a range of expansion factors controlled by the anodizing conditions. The faradaic efficiency of oxide formation is influenced by the applied potential or current. Thus, ordered porous films fall into a range of forming potentials and currents.

In the most recent dissolution research Su et al. propose an alternative to a self-ordering due to volume constraints. They developed an equifield strength model. The hypothesis encompasses pore initiation by pitting sites, ordering of pores by self-adjusting under a field constraint, and long range structure by coupled field and volume constraints[18,19]. The equifield strength model indicates that pit sites result from field enhanced dissolution. A single pit site will grow until it abuts an adjacent pit site. The boundary between pits adjusts while maintaining a fixed field strength based on the pore geometry. They identify the dissociation of water at the oxide surface as having a key role in the porosity.

1.4.2 Mechanical Deformation and Flow

Although dissolution has received the bulk of research efforts for several decades there is mounting evidence indicating the significant role of mechanical deformation and flow in the formation of porous oxides. In 2006 Skeldon et al. and Garcia-Vergara et al. performed the first material tracer study to investigate anodic alumina growth[20,21]. The group demonstrated that a thin sputter-deposited layer of tungsten between two layers of aluminum was not lost to the electrolyte during anodizing but instead was incorporated

into the film. The distortion of the tungsten band proved oxide flow in the barrier layer not only occurred, but is a significant factor in porous film evolution. The presence of an established velocity profile in the barrier layer clearly demonstrates the flow of oxide in the pore base is separate from volume expansion induced flow proposed as a self-assembly mechanism. Subsequent studies by the same group have employed tracer elements with a range of mobility with respect to aluminum[21]. The methodology remained the same for tracer studies using hafnium, molybdenum, and neodymium. The group found that tracer elements having a higher mobility in the barrier layer than aluminum are lost to the electrolyte and those with lower mobility remain in the film as a distorted band of material. From the behavior of tracer elements some important deductions about the behavior during alloy anodizing can be made. Those alloying elements having higher mobility than aluminum ion are expected to be entirely ejected and lost to the electrolyte. Those alloying elements have lower mobility in the barrier layer are expected to form oxide and act as contaminants in the alumina film.

Houser and Hebert have worked extensively to model the tracer studies of Garcia-Vergara et al.[7,22]. They showed that in steady growth of the porous film a high field conduction law and a space charge in the oxide were necessary to obtain a result consistent with the tracer studies. The modeling of steady growth films presents important insight into the forces that maintain the fixed boundary layer thickness during porous oxide growth. They did not specifically identify the origin of porosity, but presented a qualitative review of possible driving forces including electrostriction.

In order to drive mechanical deformation and flow of the oxide there must be a driving force of magnitude sufficient to overcome the oxide viscosity. Electrostriction

may play this role. The origin of electrostriction is a discontinuity in the electric field at the oxide boundaries. The current through the electrolyte, oxide, and metal are equal but the resistance of the oxide is much greater than those of the other two materials. The result is charged layers spanning the interfaces to shield a region of high field from a region of low field. The field strength through the oxide is on the order of 10^9 $V \cdot cm^{-1}$ while across the electrolyte is 2 $V \cdot cm^{-1}$.

During anodizing, opposite charges span the boundary interfaces of the oxide. Considering a snap shot of a uniform oxide film such as that in figure 1.6 (a) the metal/oxide interface accumulates positive charge as the metal is oxidized to Al^{3+}. The positive charge on the metal is almost entirely screened by a negative charge accumulated in a region near the oxide/electrolyte interface. The charge accumulates as oxygen in water and electrolyte anions are attracted to the interface and enter the oxide as mobile charge carriers. In the limit that the field in the solution is negligible relative to the field across the oxide, the film can be considered a parallel plate capacitor. With a known potential drop or capacitance the electrostriction force can be calculated. Sato calculated film pressure as a function of thickness for three field strengths on the order of those observed in anodizing and identified film pressures capable of causing mechanical breakdown or deformation of metal oxides[23]. Figure 1.6 shows ideal parallel interfaces in (a). However, as the film grows the oxide/electrolyte interface mimics that of the bare metal. Regions mentioned as sites of enhanced dissolution create non-uniformity in the interfaces. Where the non-uniformity is a region of thinning, it will be amplified by the electrostriction pressure. The region of thinning is pulled toward the metal/oxide interface and displaces oxide material, as shown in figure 1.6 (b) and (c).

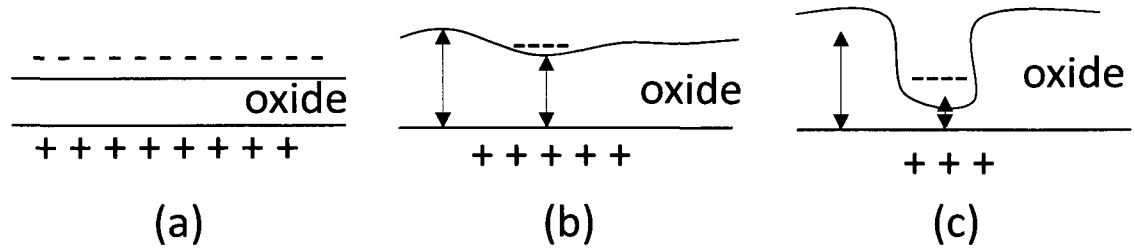

Figure 1.6: The oxide as a capacitive element during: (a) rapid uniform growth, (b) instability, and (c) pore development.

Barkey and McHugh focus on the origin of pores in anodic alumina by describing flow instability in the initially uniform oxide[2]. Special attention is paid to identify the mechanism as pattern formation as opposed to self-organization. In their model, flow instability develops in the initially uniform oxide layer that is dynamically re-stabilized by the development of pores. Pores initiate when local thinning results in an amplified electrostriction force and re-stabilize when electrostriction is balanced by viscous dissipation of the flowing oxide in the barrier layer. The most recent studies contain significant evidence supporting mechanical deformation as the origin of porous structure over a range of electric field strengths and electrostatic energy induced instability[24]. Tracer studies indicate not only flow of oxide in the barrier layer, but a developed velocity profile. An oxide viscosity on the order of 10^9 Pa-s has been suggested and a pressure gradient great enough to drive flow has been presented. The time evolution of electrical properties provides substantial evidence to support or refute this flow instability model. During the steady re-stabilized growth the resistance and capacitance provide information on the magnitude and distribution of the space charge at the oxide/electrolyte interface and on the distribution of current. If the charge is concentrated at the bottom of the pores, the capacitance will not change appreciably during the steady stage of growth. If the charge is distributed along the surface of the thickening oxide the capacitance will

decrease as the film thickens. Similarly the resistance indicates the distribution of current. If the current passes primarily through the pores, the main resistance will be in the barrier layer and not change during growth, while increasing resistance is an indication of current passing through the walls of the thickening porous layer. Although each electrical property indicates behavior dependent on the overall film thickness before pores form and the barrier layer thickness once structure develops, both properties are essential. The resistance can be calculated from previous studies where the time evolution of the potential has been recorded and it will be consistent with many of the ideas presented here. The capacitance is a necessary second property that directly describes the distribution of the space charge. Behavior of both properties must be consistent with a mechanical flow and dissipation theory to offer support.

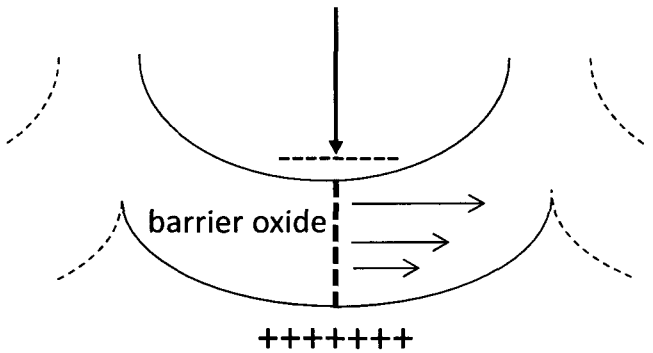

Figure 1.7: A representation of the electrostriction pressure causing flow of newly formed oxide in the barrier layer.

A working hypothesis is the initially uniform film thickness is unstable in response to any fluctuation in the film surface due to the charge spanning the interface. In the event of non-uniformity, any region of thinning is amplified as the current density concentrates in the region of lower resistance. The increased current density in turn increases a locally higher space charge and a stronger field, thus reinforcing

amplification. A pressure gradient exists between the base of the depression and a boundary that becomes the cell boundary. The pressure gradient sustains flow parallel to the metal interface, outward from the base of the indentation. The indentation becomes the pore base and the forces leading to its origin only increase as it approaches the metal interface. However, there is a volume source in the form of oxide generated at the metal/oxide interface. Oxide generation increases as the current concentrates in the indentation and the field strength increases, and new material must flow outward from the pore base through a thinning shear layer. At some fixed distance from the metal/oxide interface, the mechanical energy driving flow is dissipated by the viscous flow of newly formed oxide.

The *in situ* single frequency measurement technique that follows offers a unique view of film evolution. Two electrical properties, the resistance and capacitance, of the growing oxide film can be used to specifically identify whether the driving forces proposed in the flow instability model are responsible for the ordered porous structure observed in porous aluminum oxide films.

1.5 Technique and Theory

Two electrical properties of the growing oxide film, the resistance and capacitance, have been identified as containing critical information to the development of the film structure[1]. The practicality of the properties is lost if they cannot be considered as a function of time. In order to extract the desired properties during the growth of a film, a non-destructive technique must be applied *in situ*. A commonly used non-destructive technique to investigate films is called electrochemical impedance spectroscopy (EIS). In EIS the cell is excited using a periodic potential or current signal

with defined amplitude. The perturbation frequency is scanned over the range of 10^0-10^6 hertz (Hz). The signal may or may not be superimposed on a direct current (D.C.) bias or offset. The technique involves fitting collected impedance data using a circuit model to describe the response of the system. With an appropriate analogous circuit established, the electrical properties of each circuit element can be calculated. The drawback of true EIS is the time required to obtain a sample. The technique is best suited for probing films that are stable over the interval required for the frequency scan. In the case of the growing oxide, the capability to sample at short time intervals is imperative as the electrical properties evolve rapidly during the film growth. A single frequency EIS technique has been employed *in situ* to study the breakdown of oxide films and the effectiveness of organic coatings[25]. This technique eliminates the frequency scan and instead can be used to estimate the electrical properties as a function of anodizing time.

In order to calculate the electrical properties from collected current and potential data, an appropriate circuit is needed to describe the growing oxide. The electrochemical cell operates by controlling the current across the metal/oxide interface of the growing oxide. It can be assumed that the short lengths of well insulated wire used as connectors do not contribute to the overall circuit. The connection to the working electrode is made by silver brushes on a nickel rotator which again can be assumed to have negligible resistance. The system of interest is the electrochemical cell. The counter electrode is a material that is nonreactive in the electrolyte. The surface area of the counter electrode is significantly greater than the surface area of the aluminum and aluminum alloy samples. Based on the aforementioned, it is assumed any resistive or capacitive contribution of the counter electrode interface is negligible and omitted from the overall circuit. Based on the

chemical nature of the growing oxide film, it is the dominating contribution to the overall circuit. As a material aluminum oxide is a poor conductor of current, but is efficient at maintaining an electrostatic field through polarization of the Al-O bonds. These material properties lead to a general circuit model as is shown superimposed on a cross-section of a cell in figure 1.8.

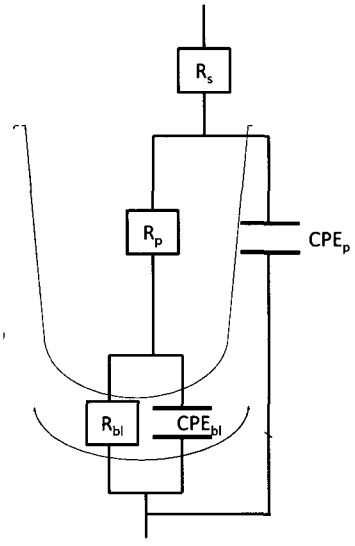

Figure 1.8: General circuit of porous films displaying resistances R and constant phase elements CPE of the solution (s), pore (p), and barrier layer (bl).

The general circuit model assigns resistances to the solution, electrolyte filled pore, and barrier layer, indicated in the figure by R_s, R_p, and R_{bl}. The general circuit model also contains two constant phase elements, CPE, one assigned to the oxide comprising the pore wall and one to the barrier layer. The term constant phase element is used to lump the non-idealities of capacitive elements in real systems. Ideal capacitors cause a phase lag between current and potential of 90°, but in real systems capacitors function with a constant phase lag that is different from 90°. The general circuit model can be simplified by systematically removing the compound circuit elements based on the operating conditions of the cell. The resistance of the solution, R_s, is eliminated by choosing a

highly conductive electrolyte. The conducting liquid phase in this study is 1.5 M sulfuric acid. The resistivity of this electrolyte is on the order of 10^1 ohm-cm, whereas in comparison, the resistivity of aluminum oxide is on the order of 10^{14} ohm-cm. Thus, the series electrolyte resistance is assumed negligible, a result that is demonstrated numerically in a following section. The flow instability model indicates the current density, space charge and electric field are concentrated in the region of thinning oxide that becomes the pore base. This assumption, and the high conductivity of the electrolyte filling the pores simplify the general circuit to a single parallel RC circuit model.

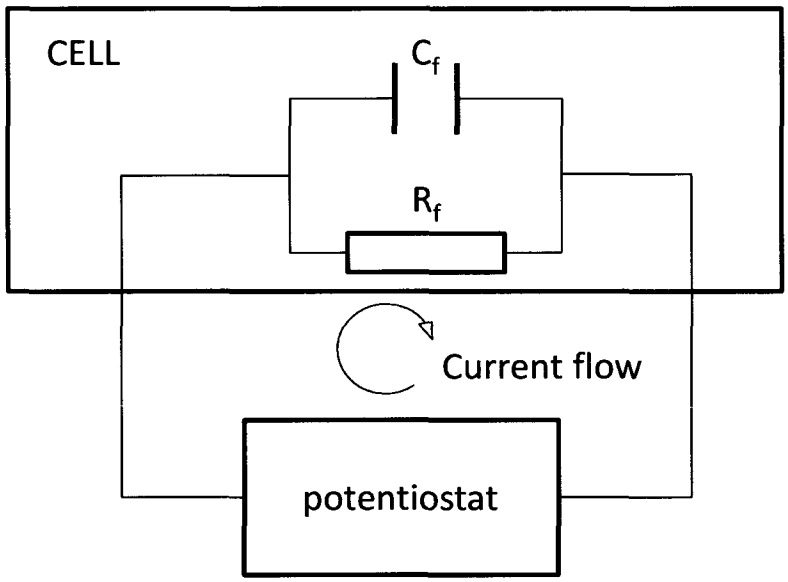

Figure 1.9: The complete circuit simplified to assign a parallel RC circuit to the film.

1.5.1 Signal Analysis

The general circuit model has been simplified to one parallel combination of a resistance and capacitive element at the barrier layer. This layer is comprised of the two interfaces indicated in figure 1.4, the metal/oxide and the oxide/electrolyte. With a low enough frequency chosen for the periodic excitation, the single frequency method

outlined above, when used in tandem with the simplified circuit in figure 1.9, describes the electrical properties of the barrier layer oxide at each pore base.

It is desired to collect information about the time evolution of electrical properties in a growing film. In turn the electrical properties will be discussed in reference to proposed mechanisms of porous oxide growth. A single frequency EIS technique has been briefly outlined whereby a periodic signal is used to probe the growing film. In this system a mean current density is maintained at the anode with a direct current (D.C.) offset and the film is probed for the phase angle between the periodic current and potential signals. The phase angle is required to calculate the capacitance. The amplitude of the periodic perturbation was maintained at 20 % of the D.C. value in an attempt to overcome any cell noise and present a clear periodic signal. The circuit response was analyzed using a steady-state sinusoidal analysis over the sample interval. This analysis assumes that over the sample interval the capacitive element is charged to the larger direct current offset. Without charging of the capacitive element the impedance to the D.C. current is given by Ohm's Law

$$R = \frac{V_{DC}}{I_{DC}} \tag{1.9}$$

where I and V represent the imposed current and measured potential respectively. The impedance R is a measure of the resistance of the oxide layer to the passage of D.C. current. The circuit response to the relatively small A.C. perturbation is more complicated, but is simplified by the reduction of circuit elements to a single parallel RC combination. The imposed current is sinusoidal in nature and assuming a linear response of the cell to the current fluctuation, the cell potential will be periodic. The impedance to the A.C. signal is of the form

$$Z = \frac{V_{AC}}{I_{AC}} = \frac{V_m \sin(\omega t + \phi)}{I_m \sin(\omega t)} \tag{1.10}$$

where V_m and I_m represent the amplitude of the periodic signals, ω is the radian frequency, and ϕ is the phase shift of the potential signal with respect to the imposed current. For a two element parallel RC circuit the impedance is

$$Z = \frac{R_f}{1 + j\omega R_f C_f} \tag{1.11}$$

where R_f and C_f are the resistance and capacitance of the film to the much smaller probing A.C. signal. Periodic signals with invariant amplitude, phase and frequency are more conveniently represented using phase vector, or phasor, representation. Equation 1.11 written in phasor form is

$$Z = \frac{R_f}{\sqrt{1 + (\omega R_f C_f)^2}} \angle - \tan^{-1}(\omega R_f C_f) \tag{1.12}$$

This equation indicates that the impedance is a function of the resistance and capacitance of the film, the impedance is projected at an angle, $\angle$, of $-\tan^{-1}(\omega R_f C_f)$. Equality between expressions 1.12 and 1.10 allow the extraction of the desired electrical properties in response to the periodic A.C. perturbation.

$$R_f = \frac{V_m}{I_m} \sqrt{1 + \tan^2(\phi)} \tag{1.13}$$

and

$$C_f = \frac{\tan(\phi)}{\omega R_f} \tag{1.14}$$

The single frequency EIS technique and method of analysis demonstrated here allows the electrical properties of the growing film to be considered with respect to each stage of

film growth. The electrical properties give key insight into the development of the final structure of porous films by being both a qualitative and quantitative measure of the physical behavior of the growing film.

CHAPTER 2

EXPERIMENTAL

The galvanic oxidation of aluminum and aluminum alloys in high conductivity acid electrolytes results in highly ordered porous films. The driving forces responsible for the nano-scale ordered structure are not well understood. Two electrical properties have been identified as containing information about the location and distribution of the current, space charge and electric field.

A data acquisition device was used to collect current and potential data for a controlled galvanic electrochemical cell. In order to investigate the charge distribution and electrical behavior of growing aluminum oxide films, the current density, temperature and material composition were varied.

2.1 Definitions

The electrochemical cell is a circuit comprising two electrodes separated by a conducting electrolyte and connected through an external power source. Galvanic oxidation is a technique wherein the current through the cell is controlled. The working electrode is where key electron transfer occurs. The counter electrode acts as an interface where reduction takes place thus completing the circuit. A third electrode, the reference, is used to measure the potential of the working electrode relative to a non-participating and therefore steady potential reference. The open circuit potential is that measured when there is no current flow through the cell.

In this study the working electrode was a rotating cylinder electrode (RCE). As the term anodizing indicates, the electrode of interest was the anode, where oxidation occurred. In this study the reference electrode was the counter electrode. Thus, all potentials were measured between the working and counter electrodes directly.

2.2 Apparatus

2.2.1 Electrochemical Oxidation Cell

The electrochemical cell was made up of a jacketed glass reaction vessel, a rotating cylindrical electrode (RCE) assembly as a working electrode, a counter electrode and a thermometer. The vessel was a 125 mL hemispherical glass volume. Figure 2.1 shows a schematic representation of the cell.

The vessel had three ports. The central port accommodated the rotating working electrode. The two remaining ports were used for the counter electrode and thermometer. A Cole-Parmer Polystat circulator with an ethylene-glycol thermal fluid was used to maintain a bulk electrolyte temperature.

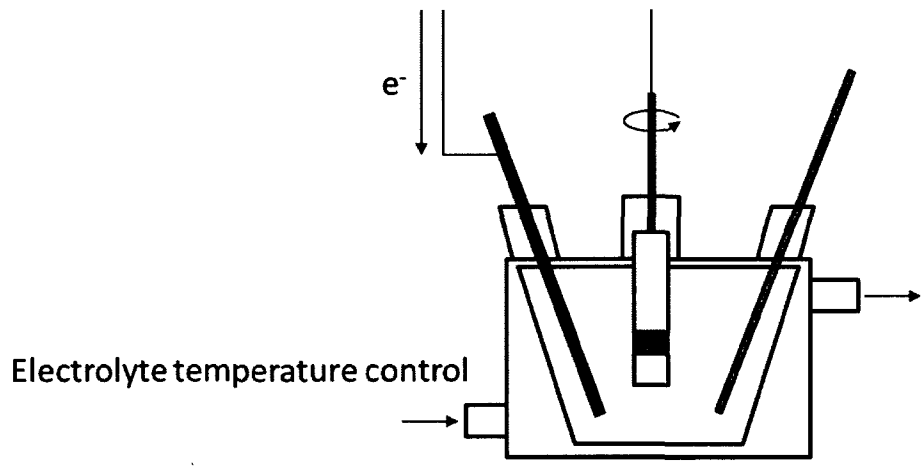

Figure 2.1: A representation of the electrochemical oxidation cell, or anodizing system.

2.2.2 Rotating Cylindrical Electrode (RCE)

The RCE is a hydrodynamic working electrode used to control convective mass and heat transfer in the cell. The principal advantage of this type of electrode is the ability to use prefabricated cylindrical samples of variable surface areas. The adjustment of rotating speed leads to control over boundary layer thickness; rotation rate was not employed in this fashion for this study. The working area of the electrode is axis-symmetric perpendicular to the axis of rotation. The RCE assembly is a Pine-Instruments Model AFE3M shaft with an ACQC01205 RCE mount consisting of a Teflon outer housing and spacers and a Nalgene threaded cap.

2.2.3 Counter Electrode

Two types of counter electrodes were used in this study. One was an inert carbon graphite rod, cylindrical in geometry. The other was comprised of 99.99 % Aluminum foil, cut to rectangular dimensions small enough to fit in the cell.

The reference electrode was shorted to the counter electrode outside the electrochemical cell. The counter electrode material is non-reactive in the electrochemical cell; it acts as an interface for the transfer of electrons. In the sulfuric acid system used in this work the reduction reaction at the counter electrode is hydrogen ion to hydrogen gas. The reaction is that of the normal hydrogen electrode (NHE) used as a standard reference potential of 0.00V. All potentials reported are those measured between the working and counter electrodes.

2.2.4 Electrode Rotator Unit

A Pine Instrument AF MSRX Electrode Rotator was employed. Connections to the shaft of the RCE were made by silver carbon brushes; there were four contacts. The

rotation rate was controlled using an auxiliary Pine MSRX Speed Control unit. A constant rotation speed of 1500 rpm was used for this study. The choice of rotation speed was limited by rotator shaft stability and chosen to provide ample convection to eliminate concentration and temperature gradients. Industrial anodizing processes employ agitation independent of the working sample due to process and geometric restrictions. The chosen experimental setup provided reliable electrical connection to the anode, surface area masking and agitation in one apparatus.

2.2.5 Potentiostat

A potentiostat is an electroanalytical instrument with the ability to control the current or potential to a system of electrodes while giving high frequency feedback of measured potential or current response. The potentiostat used in this study was a Princeton Applied Research ParStat 2273. The current and potential ranges are 2 Amps and 10 Volts respectively. A voltage divider was inserted between the potentiostat and the cell such that potentials up to 100 V were possible. The voltage divider outputs a potential to the potentiostat that is 1/10 of the actual cell potential. Potentials greater than the unadjusted 10 V range are routine in anodizing processes. The potentiostat was controlled using a combination of Princeton-supplied PowerSuite software and a National Instruments (NI) SCB-68 input/output (I/O) interface. The external input to the potentiostat was controlled by a LabView Virtual Instrument (VI) developed in house. This VI allows the user selection of: type of waveform, frequency, offset and amplitude for each signal. The output is a combination of the two selected waveforms. This study was completed using only a combination of sinusoids. The first wave had amplitude of

zero and was therefore the direct current offset or bias. The second wave is the alternating current perturbation used to collect capacitance information.

2.2.6 Data Acquisition

Data acquisition was accomplished with a National Instruments NI-DAQ USB-6211 data acquisition interface. A second virtual instrument developed in house was used to control the acquisition and output desired parameters. This VI was tailored to collect data over 10 cycles of the imposed A.C. signal. Those cycles were analyzed for the current and potential D.C. offsets, RMS values, positive and negative peaks, frequencies, and phase shifts. These parameters were used to investigate the electrical properties of the film during growth. Data collection was performed every 500 ms at a sampling rate of 125 kHz.

2.3 Materials Preparation

The preparation process for aluminum and aluminum alloy samples started with etching in 40°C solution of 50 $g \cdot L^{-1}$ sodium hydroxide. This initial etching was not appropriate for the 2024 alloy. Chemical attack on certain alloying elements left pitting that was undesired. Etching may also increase the surface concentration of alloying elements. In the case of 2024, sodium hydroxide etching was skipped. Both etched and non-etched samples were rinsed thoroughly in pure water before being ground at 1500-3000 rpm with 1000 grit silicon carbide (SiC) paper. This rough grinding proceeded until the oxide layer was fully removed and the surface appeared uniform to the naked eye. Samples were again rinsed thoroughly. Samples were polished at 3000 rpm with Struers 9 μm diamond polishing suspension and a heavy cloth. The polished samples were degreased in acetone for 15 minutes after the polishing suspension and fine material was

removed with water. Degreasing in acetone was necessary to promote even surface wetting and ensure uniform oxide growth. All samples were agitated in a 50 % by volume solution of nitric acid and water. This process is more important for alloys as this stop aids in removing alloying elements that are concentrated at the sample surface as a result of the sodium hydroxide etching. After nitric acid treatment samples were rinsed in flowing ultra-pure water for 15 minutes and dried in cool air.

This method of sample preparation left a semi-uniform surface; the imperfections were on the order of 10^3 times larger than the cell diameters of the porous oxide. The oxide structure was assumed independent of the imperfections because of the relative scale.

2.4 Chemical Reagents and Solutions

Sulfuric acid, H_2SO_4 (J.T. Baker, 96.4%) and ultrapure water produced by a Millipore DirectQ 3 filtration system were used to prepare the solutions. Acetone (VWR, BDH, 99.9%) was employed to degrease samples. Nitric acid, HNO_3 (VWR International, 68.0-70.0%) was diluted with ultrapure water for a de-smutting solution.

2.5 Cleaning

The glass electrochemical cell, thermometer and carbon graphite counter electrode were cleaned by consecutively rinsing them with 50 % by volume nitric acid and ultrapure water. In this fashion all remaining alloying element or aluminum ion was removed. Prior to a trial the electrochemical cell was rinsed twice with the electrolyte.

The rotating cylindrical electrode was cleaned when necessary by rotating in acetone, nitric acid, and ultrapure water before being allowed to air dry.

2.6 Experimental Procedure

2.6.1 Experimental Conditions

All experiments were completed in thermostatic baths with temperatures of either 0 °C or 20 °C ± 0.05 °C as measured on a standard alcohol thermometer placed approximately 1 cm away from the RCE. The electrolyte was drained and the cell rinsed for each trial, thus eliminating the effect of residual metal ions. The samples were immersed in the electrolyte for variable amounts of time as electrode rotation was employed to control the temperature of the bulk fluid. Due to submerging the sample in acid, slight chemical dissolution of the naturally occurring oxide occurred. Chemical dissolution was assumed to have a no effect on structure development.

Once the temperature stabilized the cell conditions were established and anodizing performed. The galvanic oxidation parameters were controlled by entering the D.C. offset and A.C. signal properties in a LabView VI. The signal controlling VI was opened and run before PowerSuite potentiostat control software was opened. A second VI controlled data acquisition. The parameters were adjusted to collect 10 cycles of the A.C. signal at a sampling rate of 125 kHz. In order to capture the very rapid growth and structure development at high current densities, the following order of operations was necessary: 1) start data acquisition; samples that collected only cell noise and not the imposed current could be removed later; 2) start the potentiostat; this puts the instrument in an active state; 3) enable potentiostat external control; this final step sent the desired D.C. + A.C. signal to the cell via the active potentiostat. All data collection was completed by sampling every 500 ms for at least one hour.

2.6.2 Calculation of Resistance and Capacitance

The D.C. resistance (R) of the film can be calculated in ohms-cm^2 (Ω-cm^2) by using Ohm's Law and the geometric area of the electrode. Ohm's Law states the resistance is equal to the measured D.C. potential divided by the D.C. current. The capacitance can be calculated by analyzing the circuit response to the periodic A.C. excitation. A NI designed signal processing VI in LabView software was used to determine the absolute phase of each of the A.C. imposed current and the measured periodic potential response. The algorithm extracts the phase by comparing each signal to a standard reference signal. The phase shift between current and potential is calculated by taking the difference between the measured absolute phase shifts. The raw current and potential data is also recorded in packets of 4000 points per segment. This burst of raw data includes nearly 70 full cycles of each signal. Further processing of the raw data can give the phase shift in units of seconds by comparing shift in zero crossing between the signals or taking the Fourier transform and seeking the shift at the imposed frequency.

CHAPTER 3

RESULTS AND DISCUSSION

The galvanic oxidation of aluminum to produce highly ordered porous films proceeds through a multiple stage growth mechanism. In stage one, the transient stage, rapid uniform growth is followed by development of the long range porous structure. In stage two, the steady growth stage, the porous film thickens while the barrier layer remains uniform. The results presented in this section are the electrical properties of growing porous oxide films calculated from *in situ* measurements of the cell potential in response to an imposed current. The electrical properties are discussed with respect to anodizing time, charge passed, imposed current density, material composition, and temperature. The evolution of electrical properties is discussed with respect to a flow instability model in which the initially stable uniform film is destabilized by electrostriction and re-stabilized in a patterned film by viscous dissipation.

3.1 Signal Analysis

The cell current and cell potential are collected via the potentiostat by a NI data acquisition device. The sample clocks are synchronized for each channel, eliminating delay between the two channels. An example of raw data is depicted in figure 3.1. This data was collected for a current density of 25 $mA \cdot cm^{-2}$ and a geometric surface area of approximately 2 cm^2. The D.C. bias in figure 3.1 is 0.125 on a 0-100 mA scale, indicating 12.5 mA. The amplitude of the superimposed A.C. current is 20% of the D.C. offset and

the frequency is 2000 Hz. The sampling rate was 125 kHz. The two periodic signals are clearly observed and error related to insufficient data per cycle (aliasing) was avoided. The important characteristics displayed are the D.C. bias, A.C. amplitude and phase difference between the current and potential signals. The material properties of the growing dielectric make the calculation of the capacitance sensitive to the phase angle measurement. The figure displays two cycles, some noise in the potential signal (the dashed line) can be seen. The phase is extracted over at least ten cycles, nevertheless any signal noise is significant.

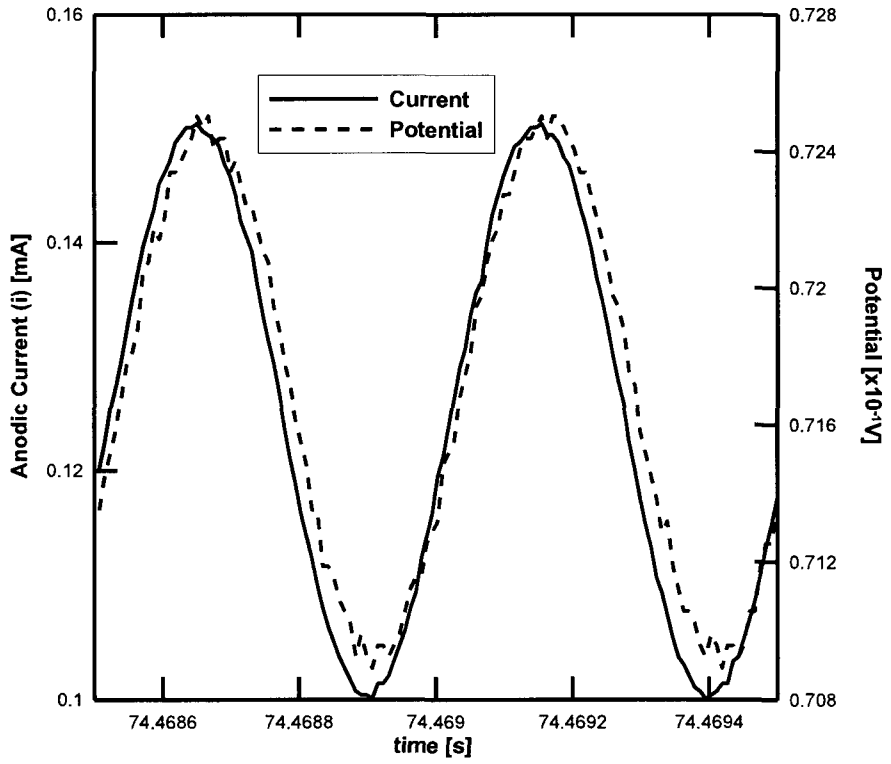

Figure 3.1: Current and potential data collected directly from the cell plotted against time.

3.2 Barrier Layer Resistance

The barrier layer resistance was taken to be the resistance to the D.C. offset calculated using equation 1.9. This resistance is indicative of porous oxide growth under

galvanostatic conditions. To simplify the general circuit model of a porous oxide displayed in figure 1.8, two arguments were presented. First, the current, space charge and electric field are assumed to concentrate in the pore base, eliminating the contribution of the pore walls. Second, an order of magnitude analysis demonstrated that the solution resistance was negligible and effectively short circuited the electrolyte filled pore. The resistivity of 1.53 M sulfuric acid at the temperatures used in this study is on the order of ohms-cm and separation between the electrodes was maintained at approximately 1 cm. At 20°C and 5 mA-cm^{-2} the potential drop between the working and counter electrode after stabilization was 12 V. For the total current of 12.5 mA the corresponding potential drop through 1 cm of electrolyte is 25 mV, or approximately 0.2 % of the total potential drop. This justifies the assumption that the series resistance of the solution is negligible. Evidence of the current and electric field concentration in the pore base can be seen in work by O'Sullivan and Wood. They demonstrated this phenomenon by analyzing the behavior of porous films when subjected to a step change in potential. The formed porous films developed a secondary porous structure at the bases of previously existing pores[12].

The resistance is calculated from the response of the cell to the imposed current, thus it is reported as a macroscopic property. Once the porous structure is established the overall resistance is assumed to indicate the behavior of the barrier layer at each pore base. Figures 3.3 through 3.26 present the resistance as a function of anodizing time and charge for three different materials, at two temperatures and four current densities. The figures are further split into two time domains, one that encompasses all stages of growth and one that focuses on the early stage.

The transient in potential during constant current anodizing is well documented. It is characterized by a rapid roughly linear increase until a peak potential is reached, then a rapid decrease to a steady value. Ohm's Law indicates that D.C. resistance calculated during galvanostatic anodizing will follow this same behavior as the potential. The explanation of the behavior is: At time t=0 there is a thin naturally occurring oxide layer. Upon imposing a current, aluminum is oxidized at the metal/oxide interface and oxygen begins migrating across the oxide. Of the ionic current approximately 60 % is contributed by anions O^{2-}, OH^{-}, and SO_4^{-2}, and 40 % by cations Al^{3+} in pure Al and alloying element cations in the alloys[6]. As the oxide layer thickens, the electrical resistance increases based on the thickness of material opposing the current flow. The resistance reaches a maximum after which time it decreases to a nearly steady value. The sharp decrease in resistance coincides with the development of major pore morphology[6]; the thickness of oxide layer that passes current is thinned to the final barrier layer thickness.

The duration of the transient stage that includes the rapid thickening followed by instability and re-stabilization in the final morphology is strongly dependent on current density. The charge passed is directly correlated to the amount of material formed by a modified Faraday's Law that includes a current efficiency. For example, to form the same amount of oxide, assuming equivalent efficiencies at each current density, takes seven times longer at 5 $mA \cdot cm^{-2}$ than 35 $mA \cdot cm^{-2}$. Films formed at higher current densities show more pronounced maxima and ensuing decreases. Flow of oxide has been shown to be more significant at higher current densities[3] where the accumulated charge on each interface is greater resulting in more stress on the film interface.

In those samples where the resistance is observed to reach a steady value only briefly before gradually increasing during the anodizing process, the incorporated acid anions may be significant. Films formed in sulfuric acid have been shown to have increased concentrations of acid anion in the film and these "contaminants" affect the viscosity of the material. Where flow of the oxide in the barrier layer is integral to the final morphology, an increase of viscosity of the flowing oxide increases the resistance to current flow.

3.2.1 Pure Aluminum

Samples of aluminum (99.99 %) were anodized in 1.53 M sulfuric acid at temperatures of 0° and 20°C. The cylindrical samples were rotated at 1500 rpm to maintain a thermostatic system and eliminate mass transfer effects. The resistance of the growing film was calculated from current and potential data collected at 500 ms intervals. The transient growth stage at each temperature was defined by a rapid increase in resistance until a peak and a decrease to a steady value. At 5 $mA \cdot cm^{-2}$ and 20°C the resistance does not peak in figure 3.4 or reach a steady value in figure 3.6. At the same current density and 0°C the resistance peaks in the transient stage and reaches a steady value before a decrease late in the steady growth stage. The decrease is attributed to a drop in the current supplied by the potentiostat and was included in order to discuss late stage transient behavior. The behavior of the curve appears to be capacitive behavior, however, it is assumed that had the film been analyzed around this late stage transient, re-ordering of the porous structure would be observed. In figure 3.9 at 35 $mA \cdot cm^{-2}$, the resistance starts increasing from a steady value after 500 seconds of anodizing. Based on Faraday's law and 100 % efficient film growth, the thickness has reached approximately

2.4 μm, meaning the aspect ratio of pore depth: diameter is on the order of 1000:1. An example of a thick film is shown in figure 3.2. In this SEM image the film is extremely thick relative to the pore diameter. This film has fractured along cell boundaries after removal from the cell, revealing the long range growth behavior in a multiple cell domain.

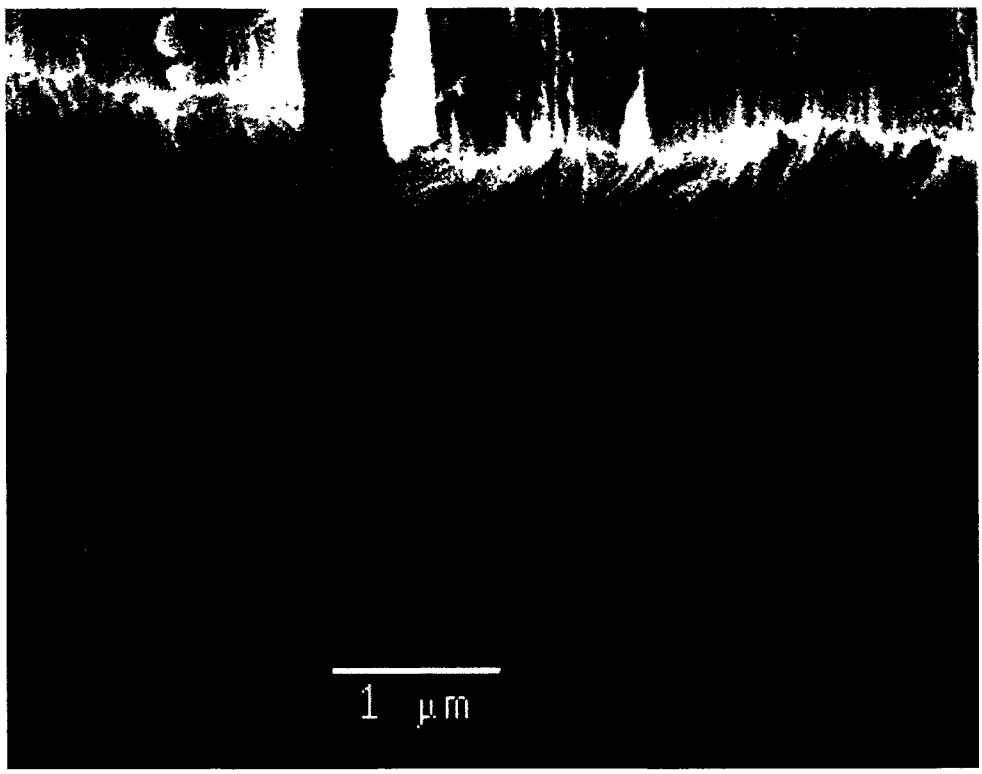

Figure 3.2: SEM image of a thick and fractured aluminum oxide film, depth:diameter ratio on the order of 1000:1.

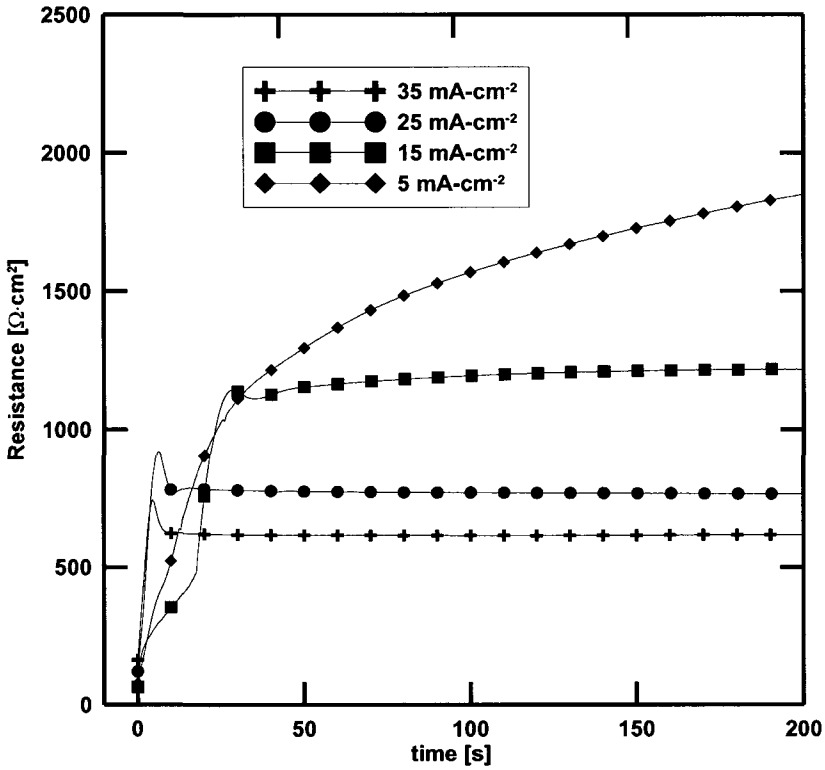

Figure 3.3: Transient stage resistance against time for Al samples in 20°C electrolyte.

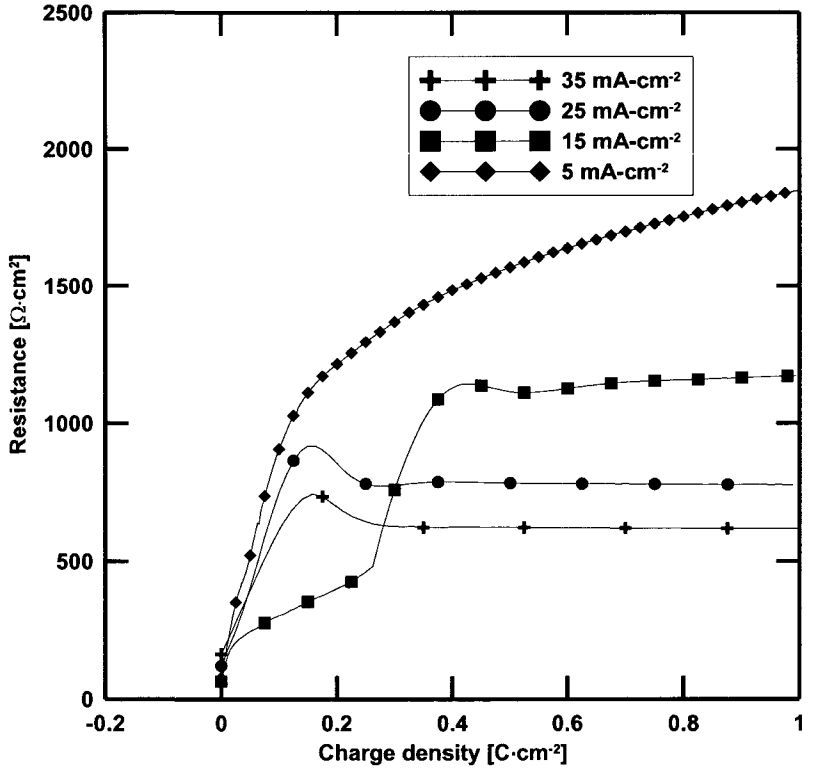

Figure 3.4: Transient stage resistance against charge density for Al samples in 20°C electrolyte.

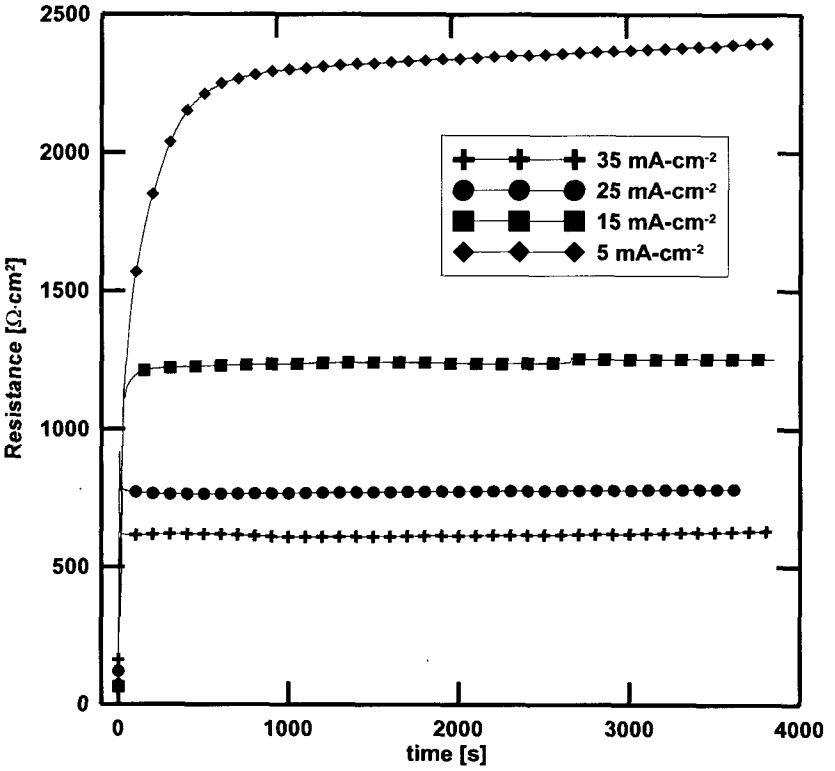

Figure 3.5: Steady stage resistance against time for Al samples in 20°C electrolyte.

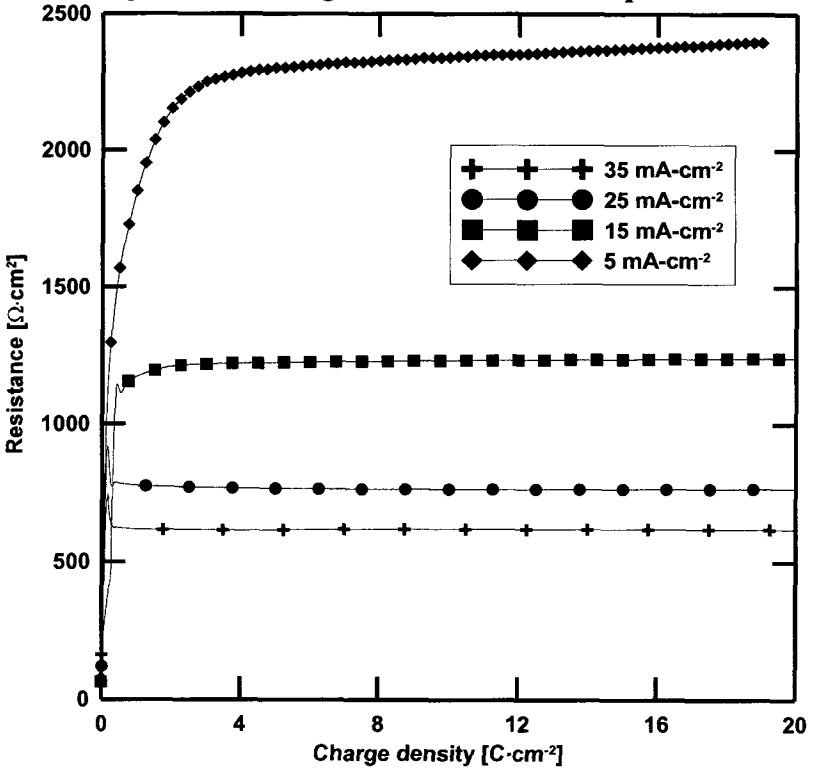

Figure 3.6: Steady stage resistance against charge passed for Al samples in 20°C electrolyte.

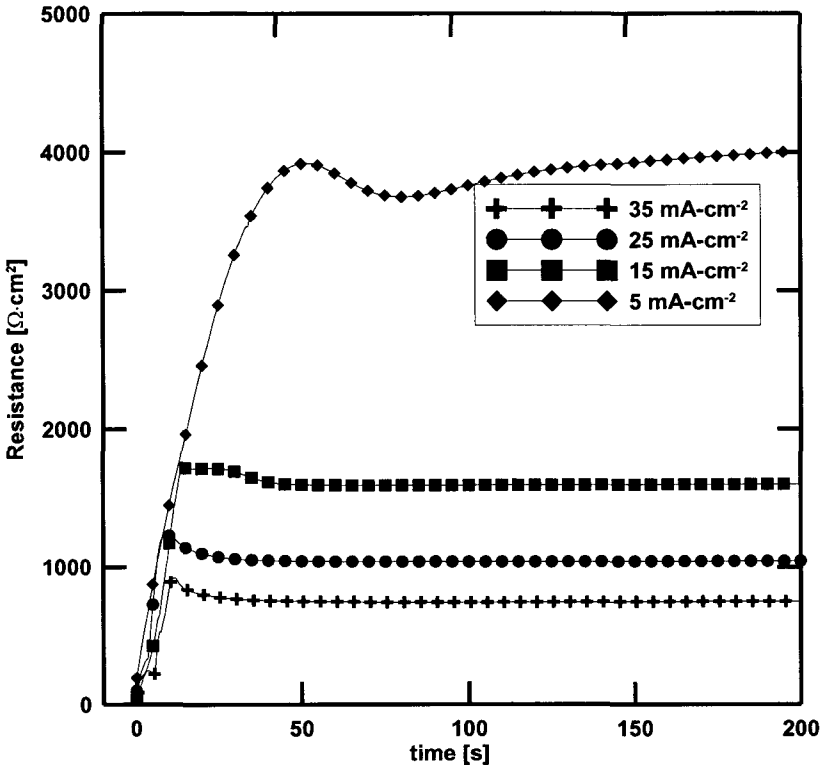

Figure 3.7: Transient stage resistance against time for Al samples in 0°C electrolyte.

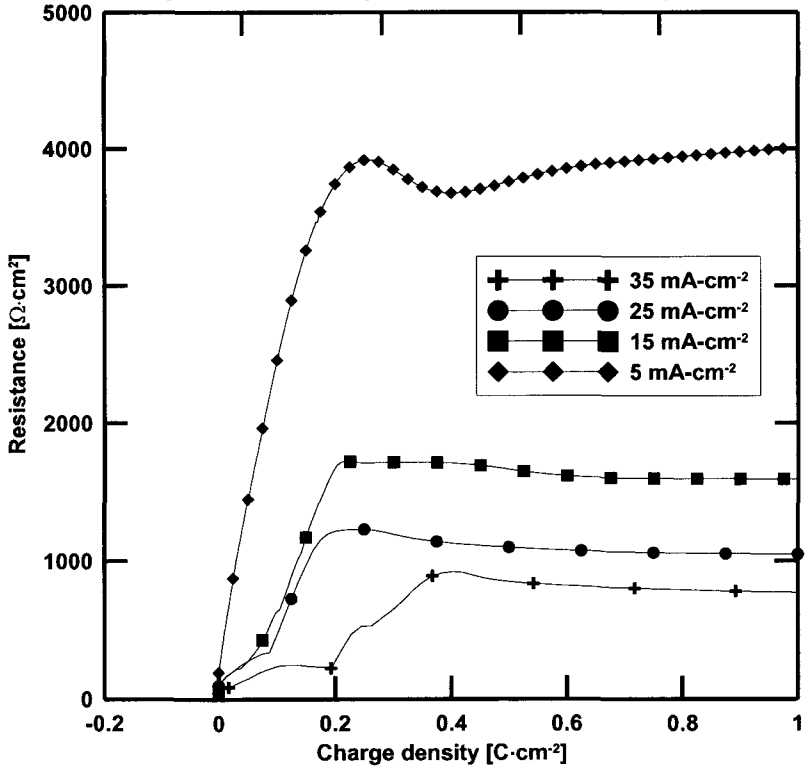

Figure 3.8: Transient stage resistance against charge for Al samples in 0°C electrolyte.

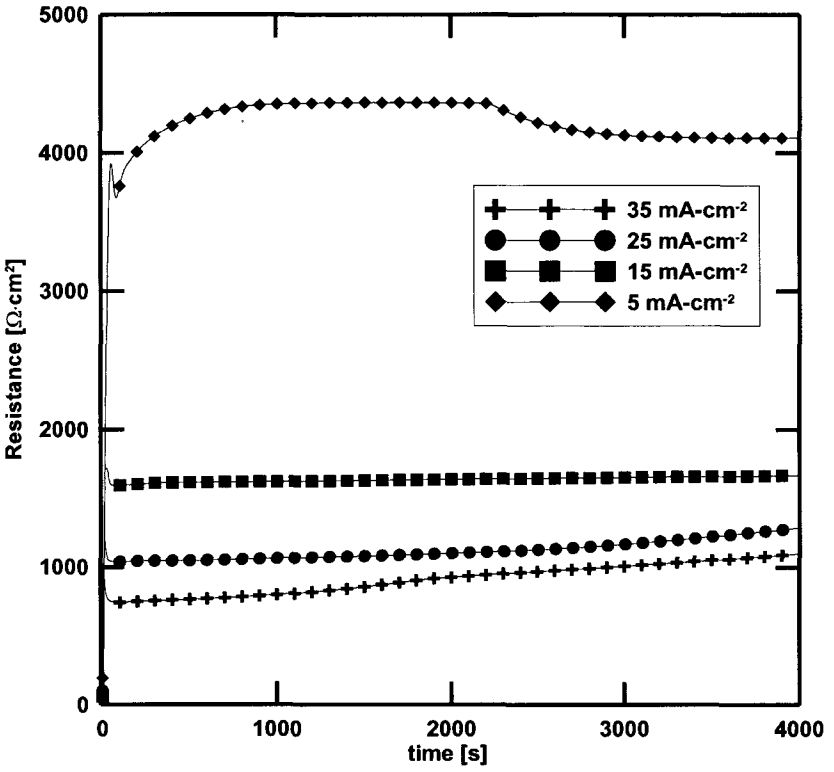

Figure 3.9: Steady stage resistance against time for Al samples in 0°C electrolyte.

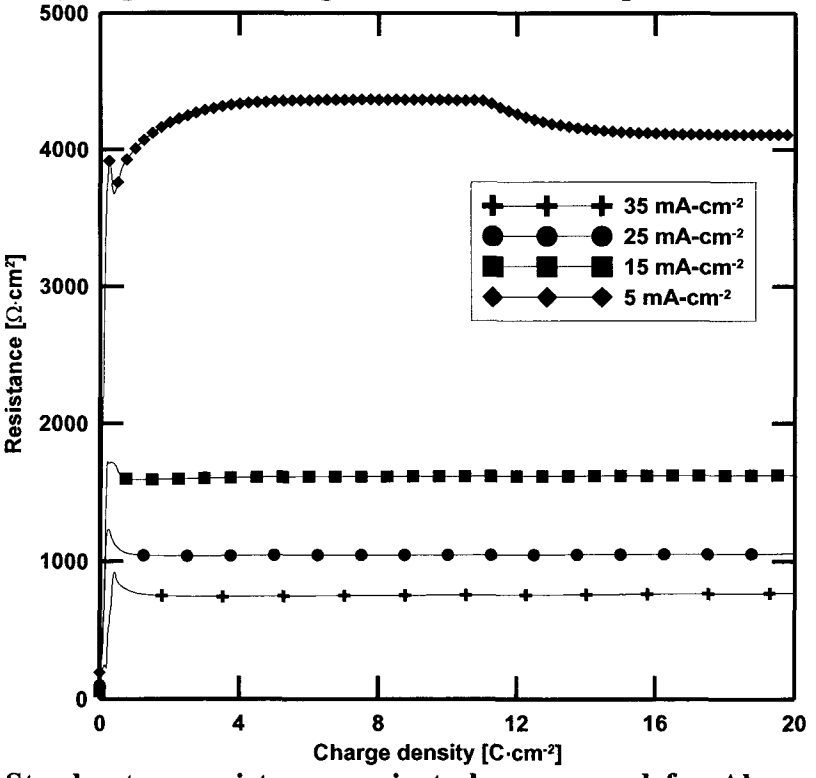

Figure 3.10: Steady stage resistance against charge passed for Al samples in 0°C electrolyte.

3.2.2 6061 Alloy

Industrially speaking, aluminum is commonly found as an alloyed material. These alloys have the advantage of better workability in regard to cutting and shaping. The alloy designated 6061 is common, the elements present in this material are summarized in table 3.1. Samples of 6061 alloy were anodized in 1.53 M sulfuric acid at temperatures of 0° and 20°C. The cylindrical samples were rotated at 1500 rpm. Figure 3.11 displays the resistance as a function of charge passed during transient stage growth. The plot demonstrates the resistance peak coincides with a certain charge passed immaterial of current density; this is strong indication that the thickness of the film is a major factor in stability. In figure 3.13 at 35 $mA \cdot cm^{-2}$ and 20 °C the film resistance begins increasing at approximately 1000 seconds while in figure 3.17 at the same current density and low temperature the transition begins earlier and is more dramatic, an indication of the effect of temperature in the late stages of film growth when the pore aspect ratio is on the order of 1000:1. Figures 3.15 and 3.16 indicate that the resistance of the film at time t=0 for current densities of 15 and 35 $mA \cdot cm^{-2}$ was elevated relative to that at the other current densities. This indicates a thicker oxide film existing at the start of anodizing. The start of oxidation was taken to be the point at which the imposed current was observed in the data output. Trials were synchronized by adjusting the oxidation time based on the observation of this current. The imposed current appeared when external control of the potentiostat was enabled. It was assumed the potentiostat step pulse to the desired current was short on the scale of the sampling interval.

Table 3.1: Alloy composition based on wt. % of each element present in measureable quantity[26].

	6061 Alloy	2024 Alloy
Component	**Wt. %**	**Wt. %**
Al	95.8 - 98.6	90.7 - 94.7
Cr	0.04 - 0.35	Max 0.1
Cu	0.15 - 0.4	3.8 - 4.9
Fe	Max 0.7	Max 0.5
Mg	0.8 - 1.2	1.2 - 1.8
Mn	Max 0.15	0.3 - 0.9
Si	0.4 - 0.8	Max 0.5
Ti	Max 0.15	Max 0.15
Zn	Max 0.25	Max 0.25
Other, each	Max 0.05	Max 0.05
Other, total	Max 0.15	Max 0.15

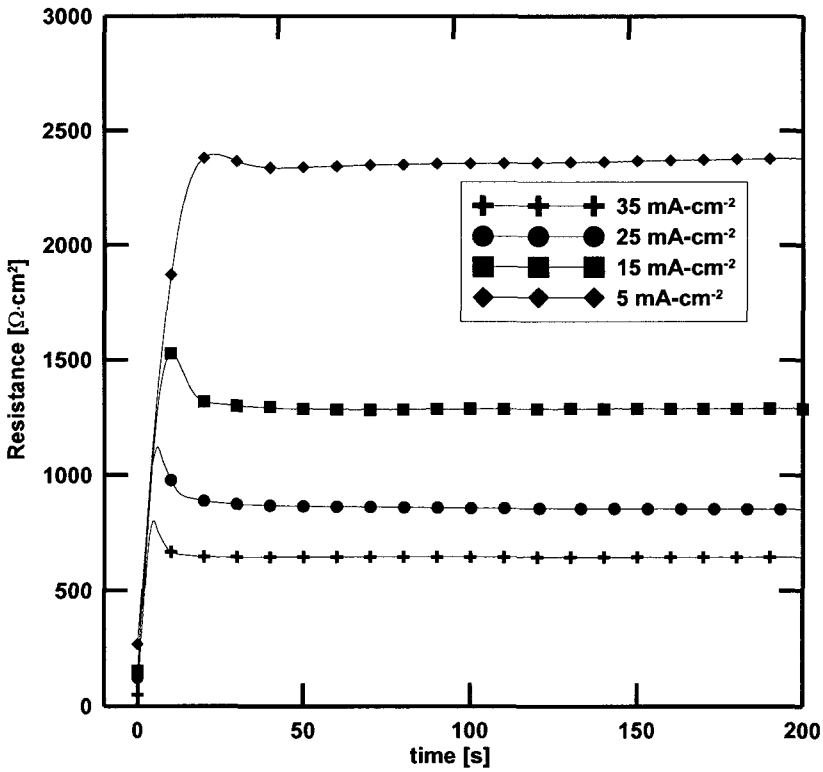

Figure 3.11: Transient stage resistance against time for 6061 alloy samples in 20°C electrolyte.

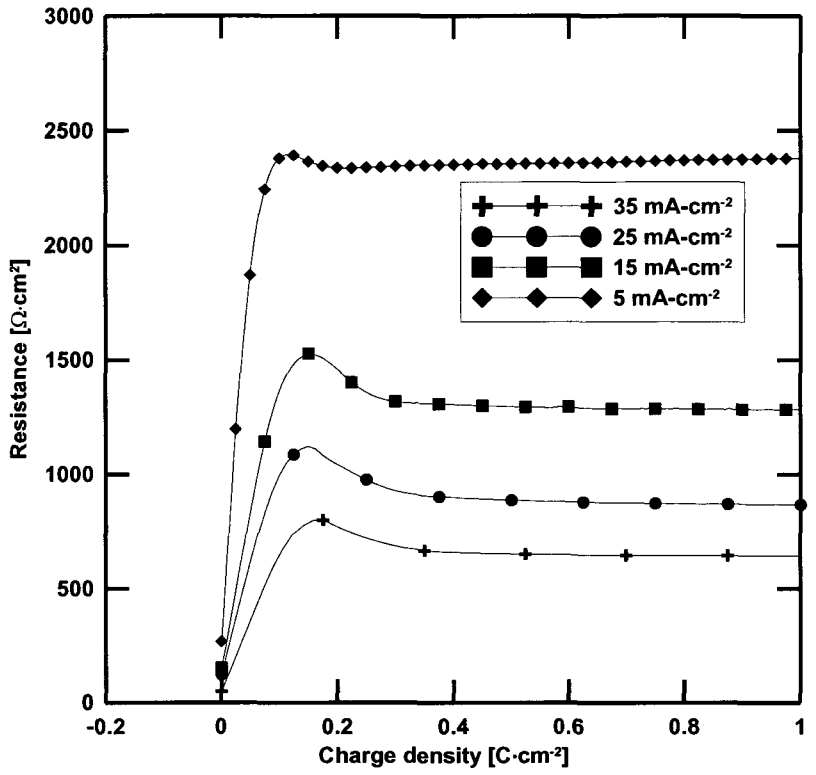

Figure 3.12: Transient stage resistance against charge for 6061 samples in 20°C electrolyte.

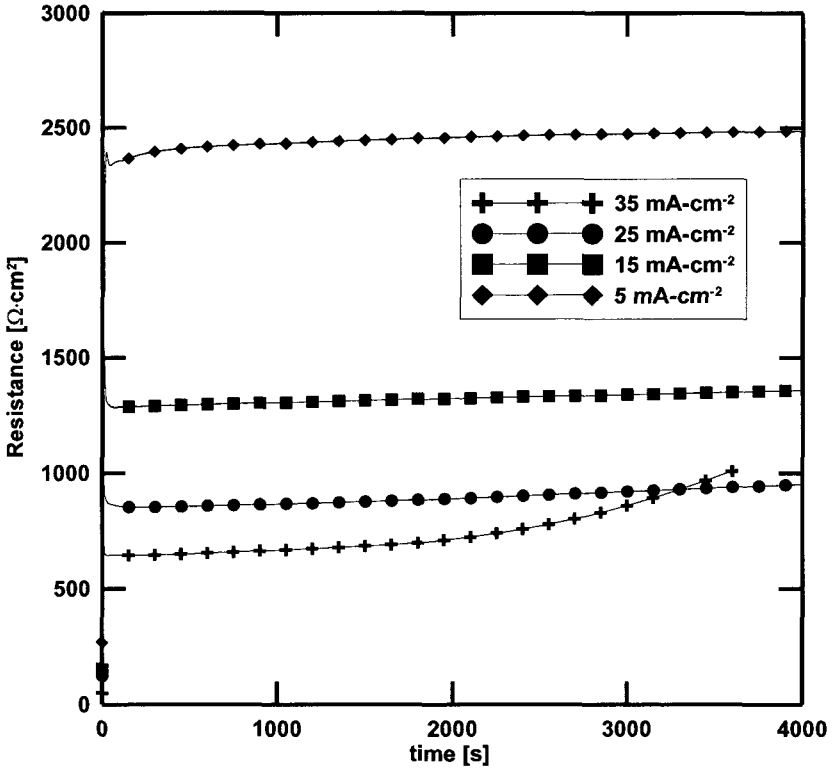

Figure 3.13: Steady stage resistance against time for 6061 samples in 20°C electrolyte.

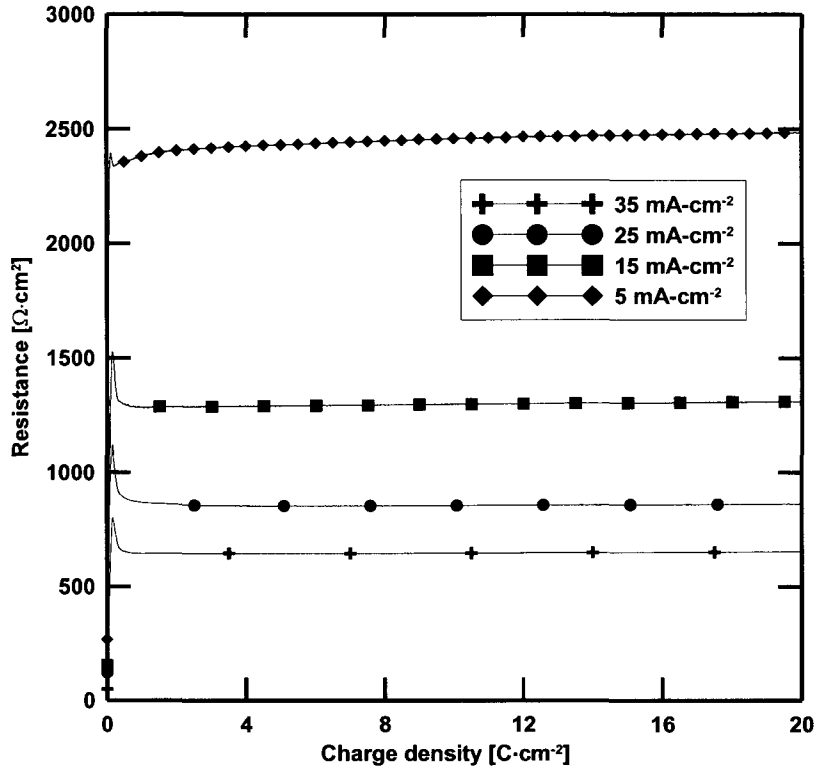

Figure 3.14: Steady stage resistance against charge for 6061 samples in 20°C electrolyte.

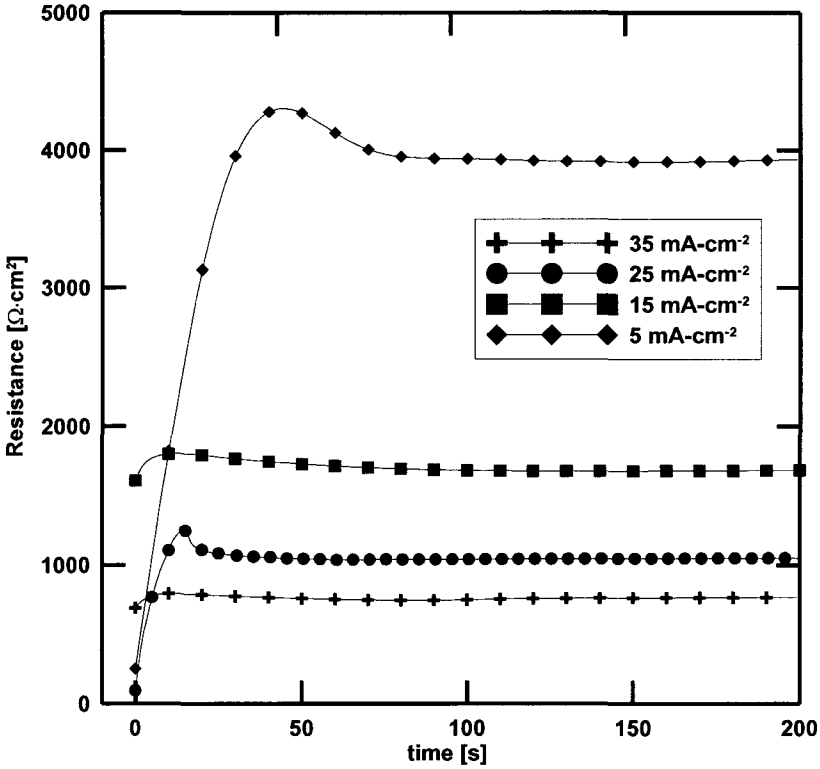

Figure 3.15: Transient stage resistance against time for 6061 samples in 0°C electrolyte.

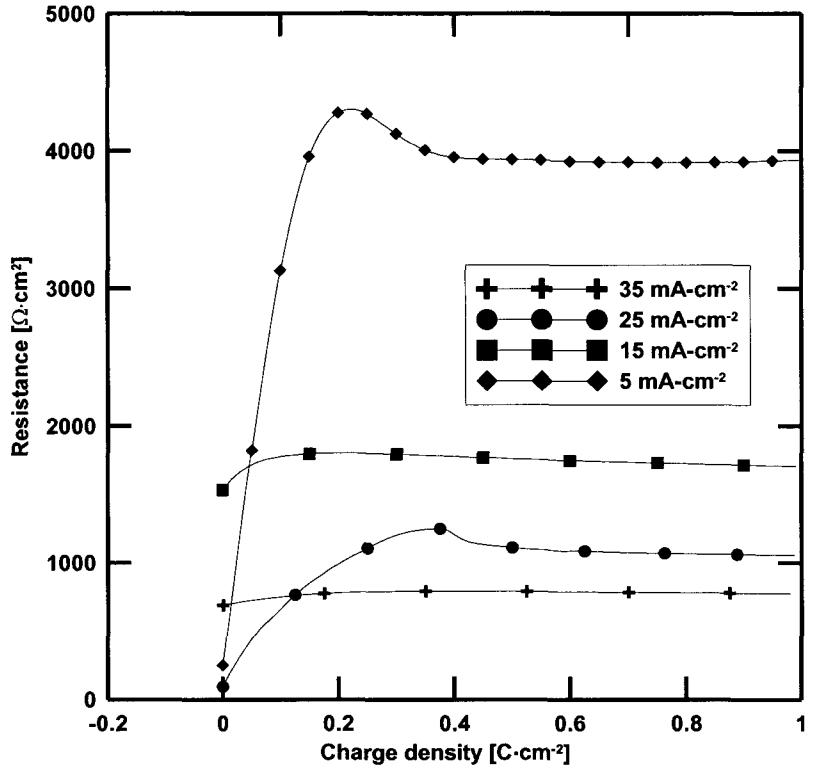

Figure 3.16: Transient stage resistance against charge for 6061 samples in 0°C electrolyte.

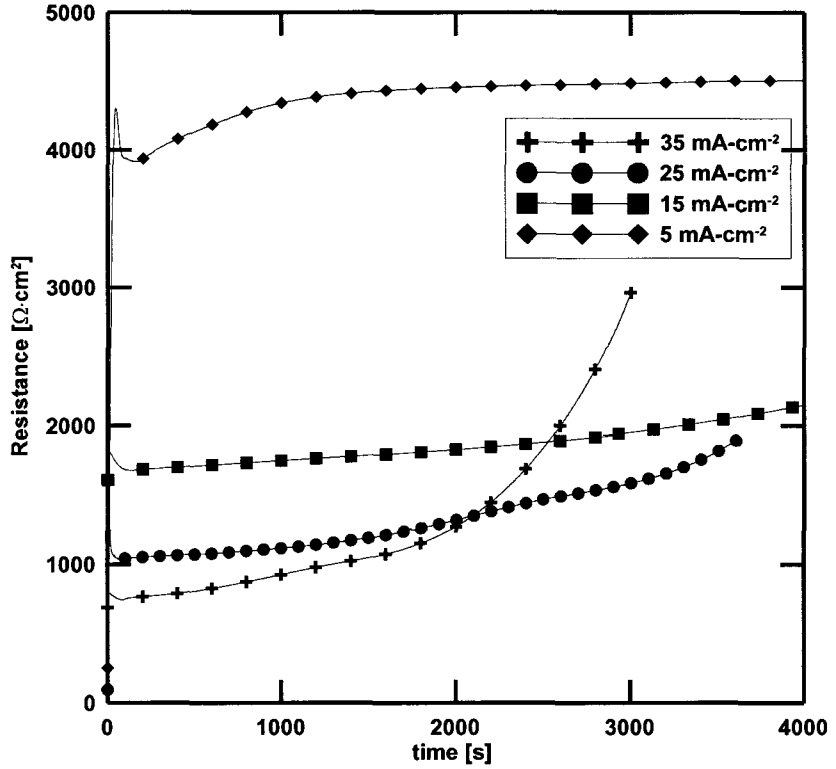

Figure 3.17: Steady stage resistance against time for 6061 samples in 0°C electrolyte.

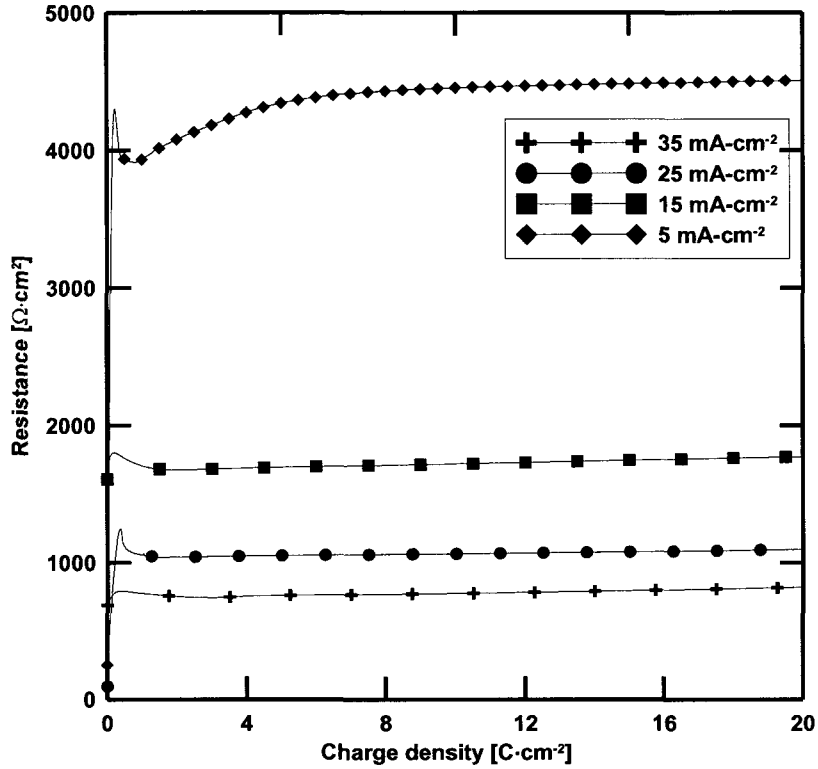

Figure 3.18: Steady stage resistance against charge for 6061 samples in 0°C electrolyte.

3.2.3 2024 Alloy

Alloys such as 2024 are used industrially in situations requiring a high strength to weight ratio. The principal alloying elements of 2024 are copper and magnesium as indicated in table 3.1. Samples of 2024 alloy were anodized in 1.53 M sulfuric acid at temperatures of 0° and 20°C. The cylindrical samples were rotated at 1500 rpm. Figure 3.20 is an immediate indication of transient behavior different from the other materials. Figure 3.24 at low temperature emphasizes the existence of multiple transient stages at each current density. The resistance of the film rapidly increases to a point, and then the rate of increase slows but remains linear with time. The second transient stage has similar behavior to the transient stages of materials previously presented, that is, a rapid increase to a peak followed by decrease to a steady value. Figures 3.25 and 3.26 indicate shorter

anodizing periods but include both growth stages of interest. At long anodizing times and high current density the resistance begins increasing as observed with other materials.

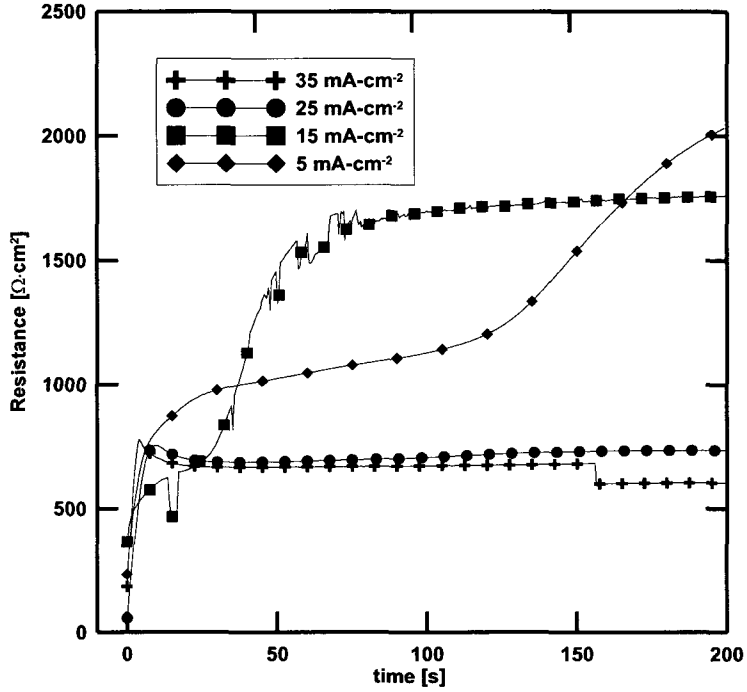

Figure 3.19: Transient stage resistance against time for 2024 samples in 20°C electrolyte.

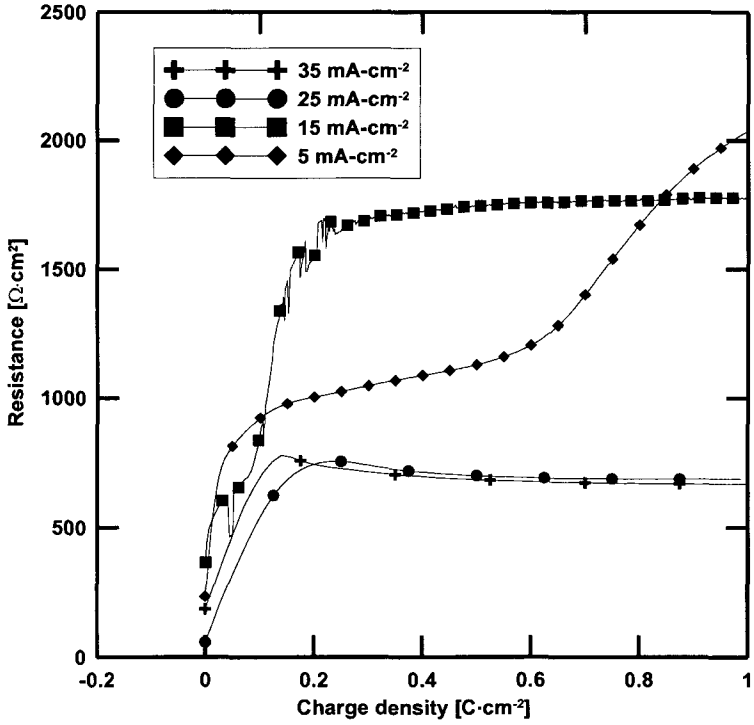

Figure 3.20: Transient stage resistance against charge for 2024 samples in 20°C electrolyte.

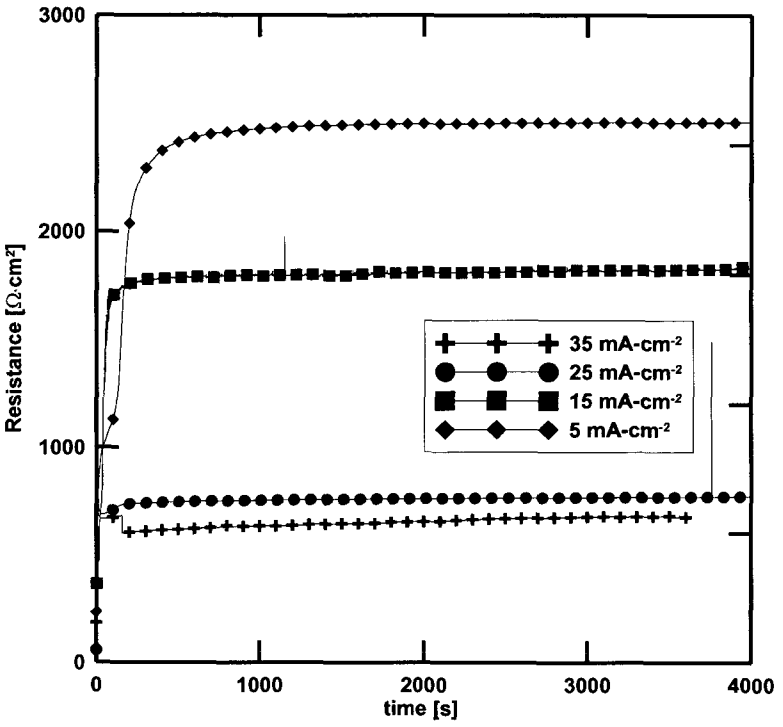

Figure 3.21: Steady stage resistance against time for 2024 samples in 20°C electrolyte.

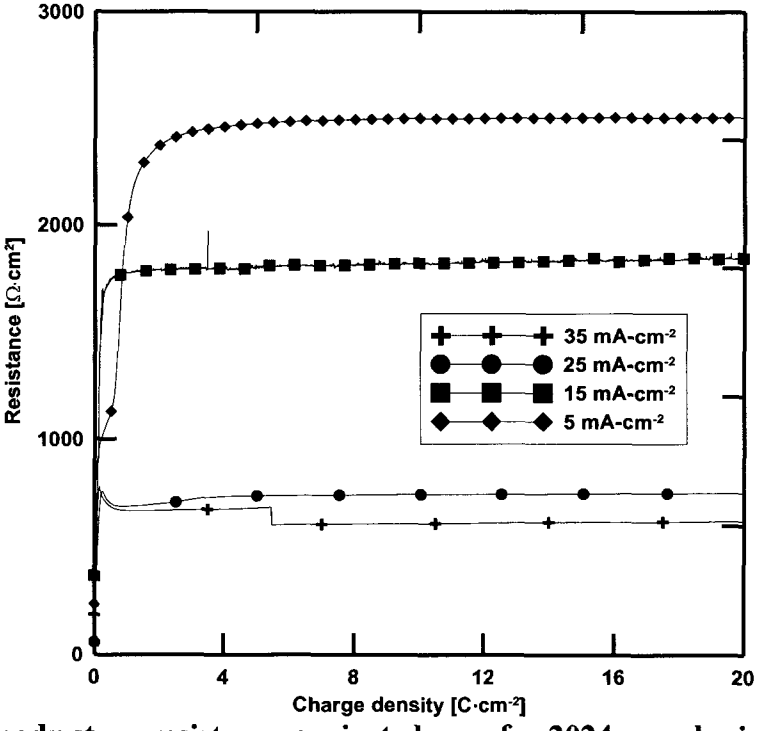

Figure 3.22: Steady stage resistance against charge for 2024 samples in 20°C electrolyte.

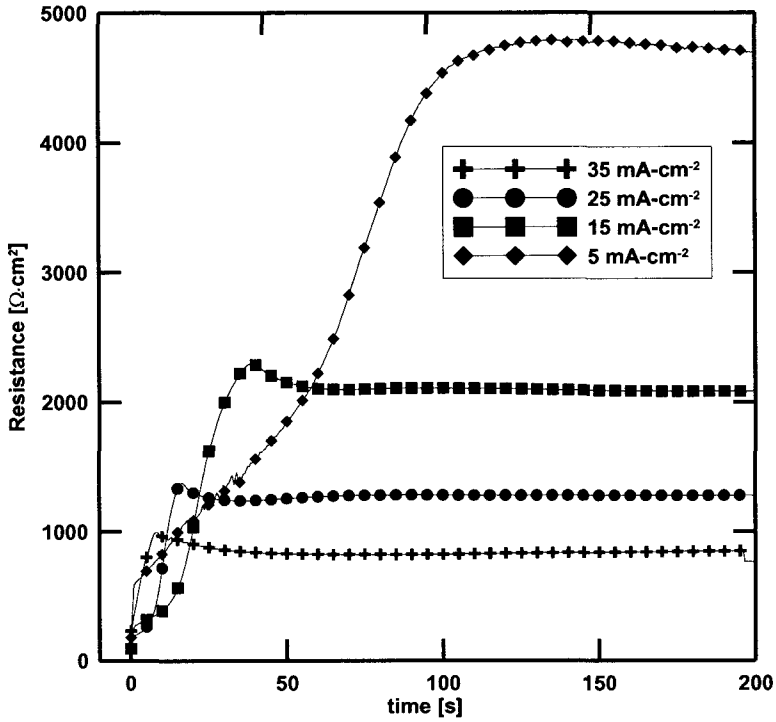

Figure 3.23: Transient stage resistance against time for 2024 samples in 0°C electrolyte.

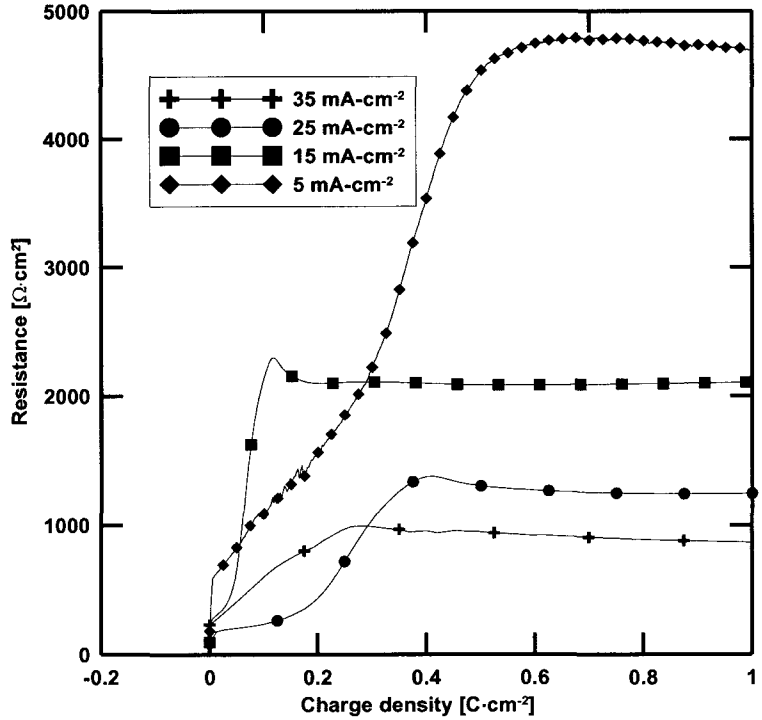

Figure 3.24: Transient stage resistance against charge for 2024 samples in 0°C electrolyte.

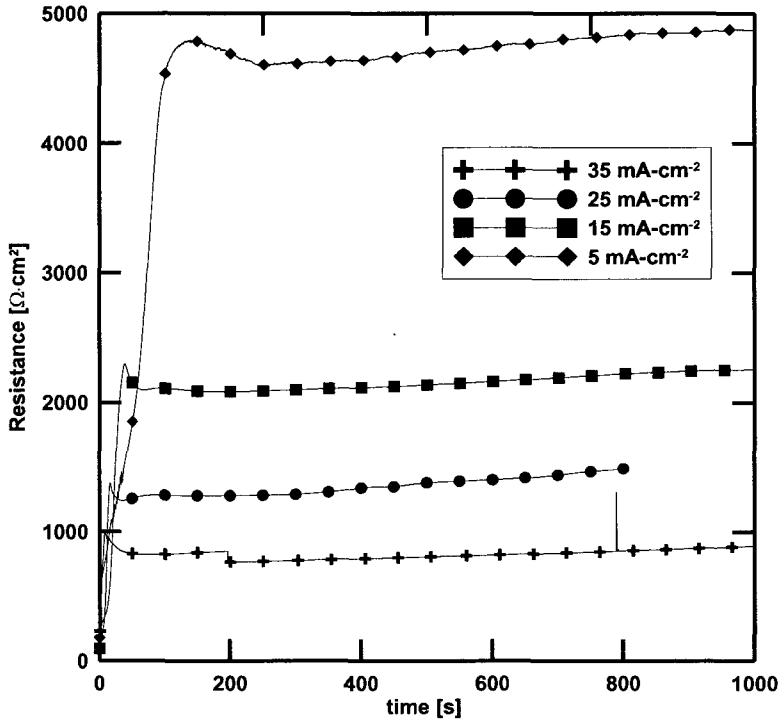

Figure 3.25: Steady stage resistance against time for 2024 samples in 0°C electrolyte.

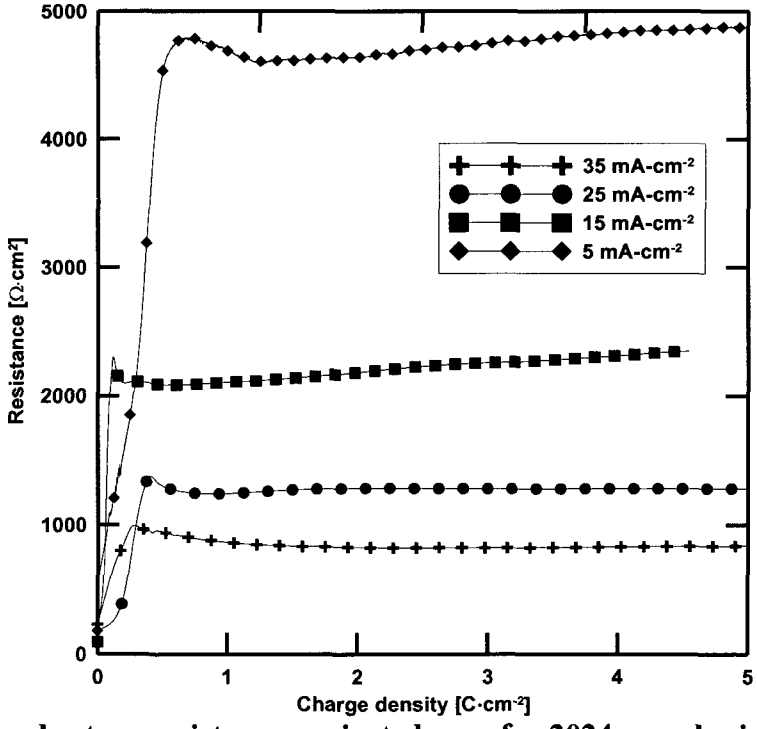

Figure 3.26: Steady stage resistance against charge for 2024 samples in 0°C electrolyte.

3.3 Capacitance and Charge Separation

Analysis of the signals independently provided the phase of each signal compared to a reference signal with a fixed origin. The phase shift between the potential and current was calculated by unwrapping each measured phase and taking the difference. Phase unwrapping is necessary to eliminate a measured phase greater than 180° or less than -180°. It is accomplished by considering each signal in a phasor representation. In capacitive circuits the current leads the potential or, equivalently, the potential lags the current. The calculated capacitance is an estimate based on the excitation of the system by a fixed frequency of alternating current superimposed on a direct current offset. As mentioned previously the electrolyte short circuits the porous films and the calculated capacitance is effectively a parallel combination of the barrier layer capacitances beneath every pore. Due to relatively small contribution of the capacitance to the overall impedance, the calculated capacitance is very sensitive to the phase difference. The pore distribution for films formed in sulfuric acid is on the order of 10^{11} pores per square centimeter. The total capacitance of a set of parallel elements is the sum

$$C_T = \sum_{i=1}^{N} C_i \tag{3.2}$$

where N is the total number of capacitors in parallel. The film can be approximated as a parallel plate capacitor and the capacitance leads to an estimation of the thickness of dielectric using

$$C = \frac{\varepsilon \varepsilon_0 A}{d} \tag{3.3}$$

Here ε is the dielectric constant of aluminum oxide, ε_0 is the permittivity of free space, A is the area and d is the separation between charges. For this study the area was assumed

to be the geometric area and the permittivity of alumina was taken to be 10. The geometric area is the surface area of the cylindrical electrode as calculated from diameter and height measurements. The total capacitance is the summation over each pore base being represented by a capacitive element. In this case the geometric area is larger than the capacitive plate area, resulting in an overestimation of the charge separation when compared to observed barrier layer thicknesses.

Oxidation of the aluminum results in a net positive metal/oxide interface where aluminum ions enter the oxide lattice and migrate towards the oxide/electrolyte interface. At the oxide/electrolyte interface oxygen in water and the electrolyte anion are attracted to the oxide surface. Electrolytes dissociate leaving oxygen and acid anions free to enter the oxide lattice. The phase shift demonstrated by figure 3.1 is indicative of the oxide layer functioning as a capacitor. As more dielectric material is formed, the capacitance decreases as the thickness of dielectric separating the charges increases. The capacitance is assumed to be a measure of the two oppositely charged interfaces being separated by the growing dielectric. In the barrier layer aluminum and oxygen ions are counter-migrating and at any sample interval the charge separation over the geometric surface is non-uniform. The barrier layer thickness increases with decreasing current density and temperature, thus the calculated capacitance should decrease with the same changes in conditions.

3.3.1 Al, 6061 alloy, and 2024 alloy

Samples of aluminum (99.99 %), 6061 alloy and 2024 alloy were anodized in 1.53 M sulfuric acid at temperatures of 0° and 20°C. The cylindrical samples were rotated at 1500 rpm to maintain a thermostatic system and eliminate mass transfer effects.

The capacitances of the growing films were calculated from current and potential phase data collected at 500 ms intervals. Although the figures indicate fluctuation in the capacitance because of the rapid sampling intervals and local distribution of charge, they show a clear early decrease in capacitance followed by a rapid increase and finally a decrease to a steady value. This mirrors the resistance behavior as capacitance decreases with increasing oxide thickness and increases as the oxide effectively thins to the separated charges during pore formation.

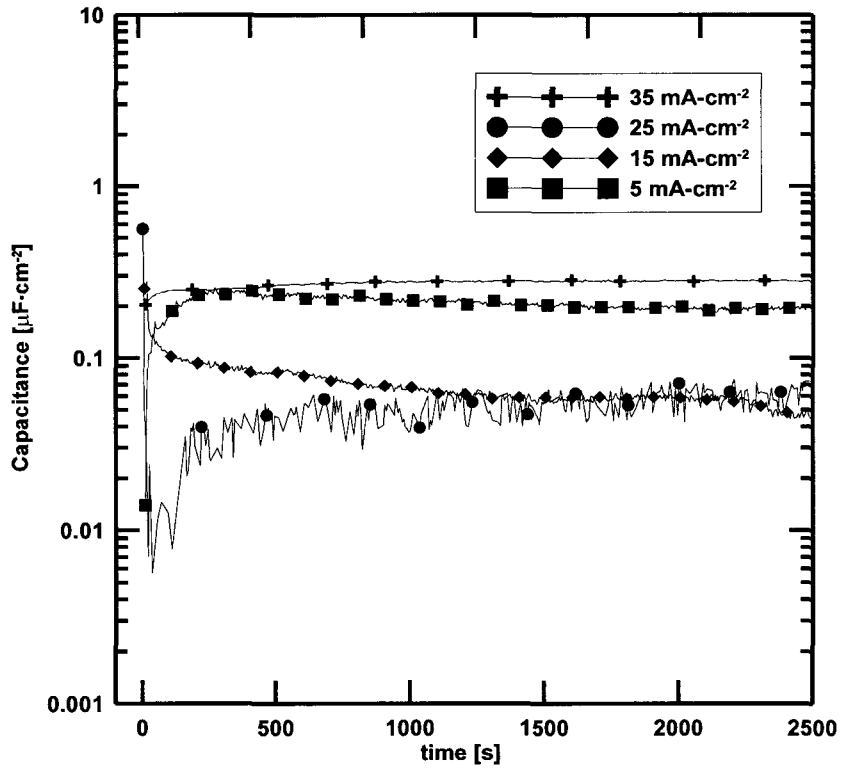

Figure 3.27: Steady stage capacitance against time for Al samples in 20°C electrolyte.

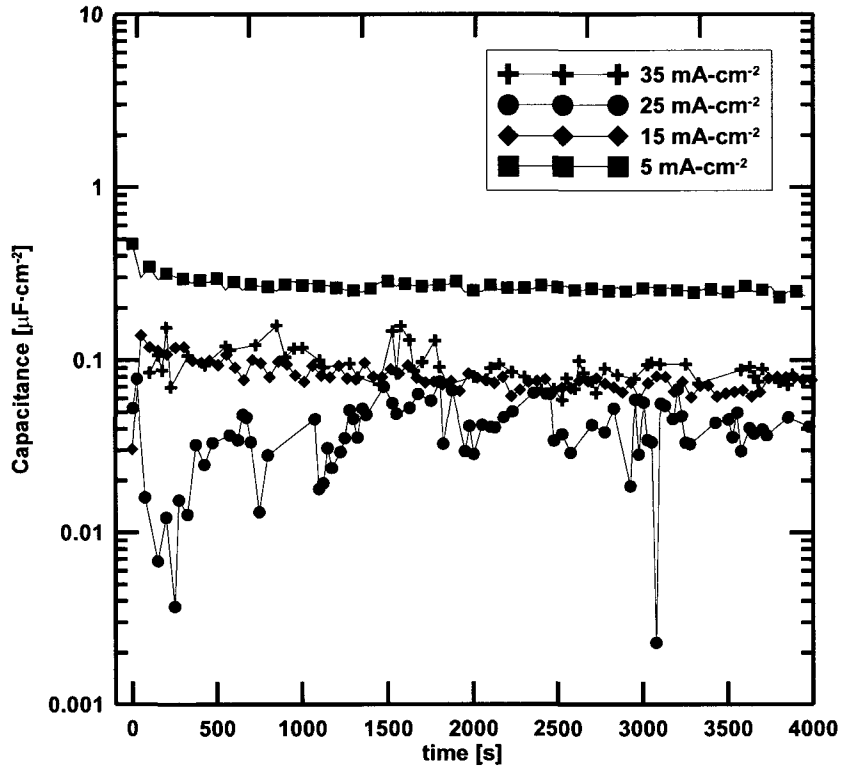

Figure 3.28: Steady stage capacitance against time for Al samples in 0°C electrolyte.

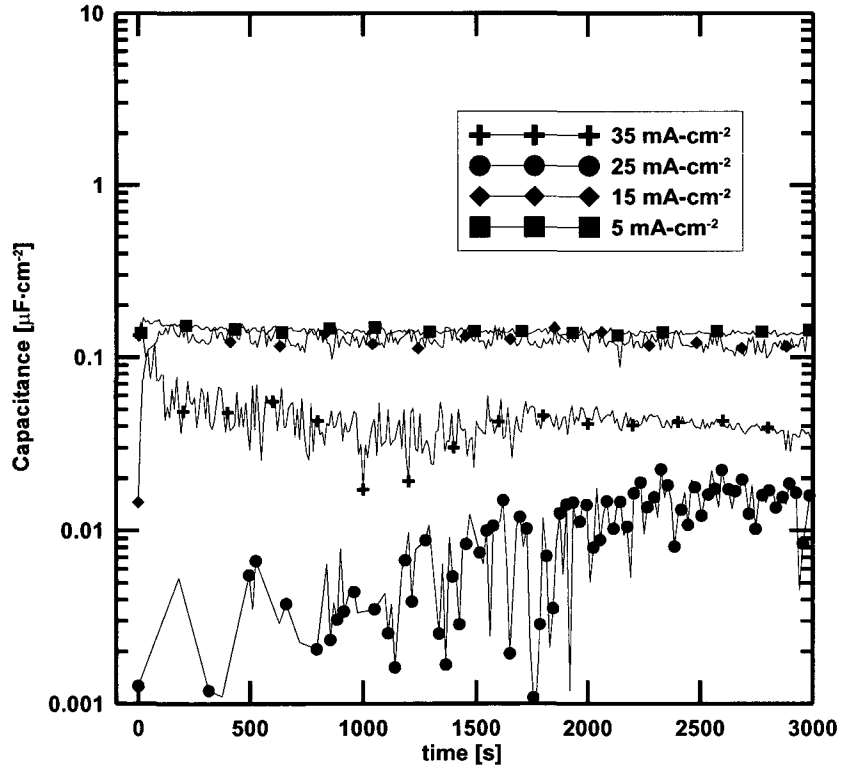

Figure 3.29: Steady stage capacitance against time for 6061 samples in 20°C electrolyte.

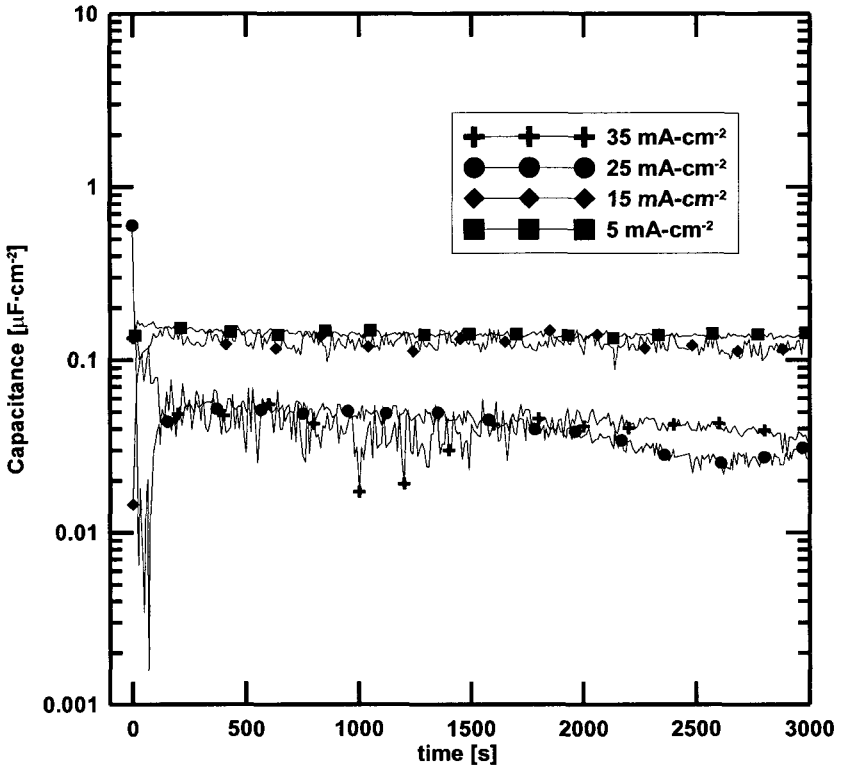

Figure 3.30: Steady stage capacitance against time for 6061 samples in 0°C electrolyte.

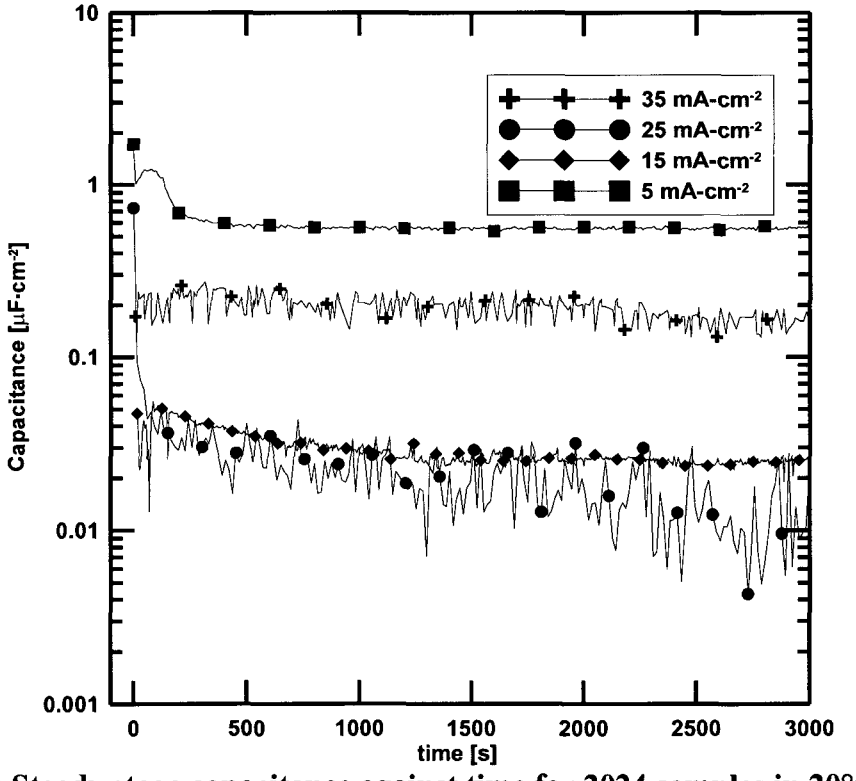

Figure 3.31: Steady stage capacitance against time for 2024 samples in 20°C electrolyte.

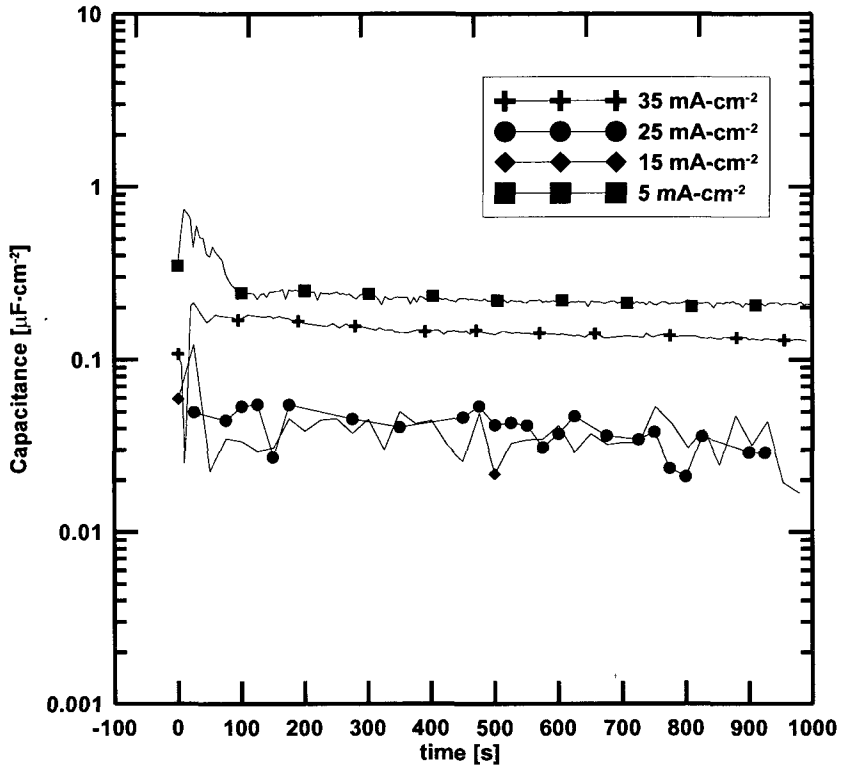

Figure 3.32: Steady stage capacitance against time for 2024 samples in 0°C electrolyte.

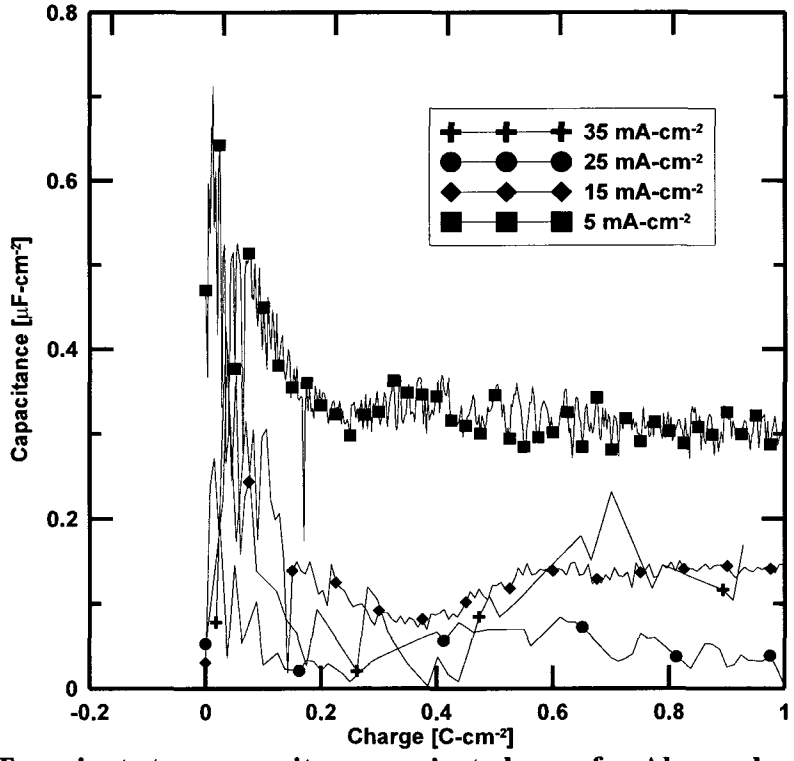

Figure 3.33: Transient stage capacitance against charge for Al samples in 0°C electrolyte.

3.4 Discussion

The objective of this study is the desire to both qualitatively and quantitatively describe the instability that leads to pore development and the forces that dynamically re-stabilize the film in its steady growth structure. Two electrical properties of the growing film, the resistance and capacitance, have been identified as highly descriptive of the evolving film and measurable during growth. The use of an *in situ* single frequency technique offers the benefit of a frame-by-frame view of the growing oxide.

3.4.1 The Circuit model and Technique

The figures presented in sections 3.2 and 3.3 demonstrate the ability to acquire data during each stage of growth. At high current density the transient stage of growth may be on the order of seconds, but the *in situ* technique used for this study is capable of customization. It is more than possible to sample more frequently, even on the order of 10 ms. However, at higher sampling frequencies there is a risk of inaccurate phase estimation. The capacitance calculation is very sensitive to the phase angle between current and potential signals. Situations arose where the phase difference fluctuated between positive and negative values. A positive phase difference indicates the current is leading the potential response and is the expected behavior for a capacitive circuit. A negative phase angle indicates the potential is leading the current and is characteristic of an inductive circuit. Although the inductive behavior of oxide films has been studied, it is more likely, due to the equality of the capacitance and inductance, that this is a misrepresentation of the phase. An example of the capacitance calculated from shifting phase measurements is displayed in figure 3.34. The instrument was operated within the manufacturer's analog-to-digital conversion (ADC) capabilities but no in depth study of

instrument settling time was performed. A study of A.C. frequency and amplitude effects as well as sampling interval is included in the recommendation section. In systems where the charge separation, meant to represent the thickness of the film, calculated from the capacitance exceeds the maximum thickness possible calculated using Faraday's law, the assumption that negative charge spans the oxide/interface breaks down.

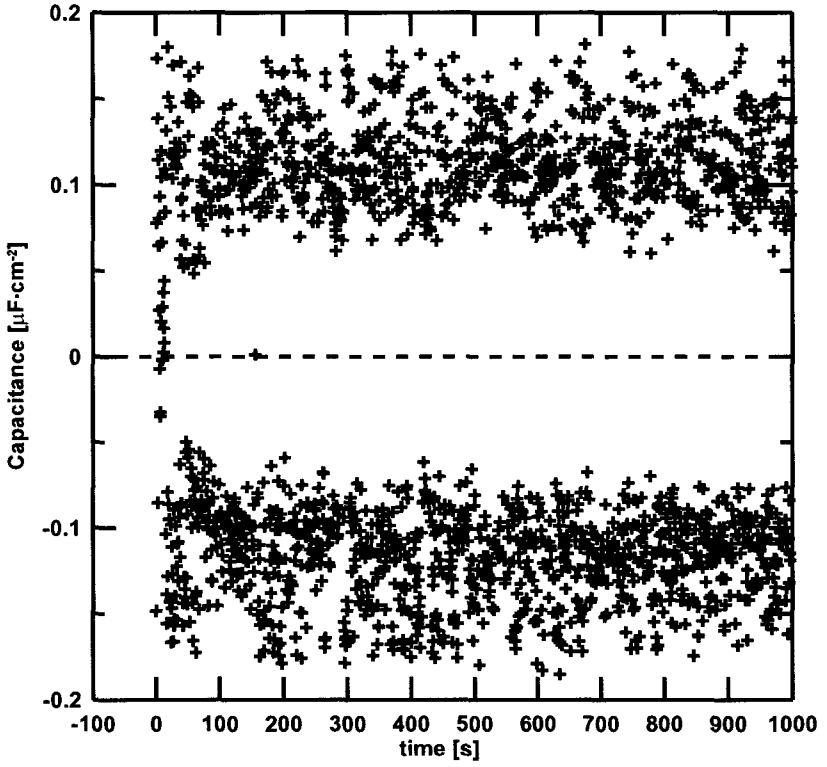

Figure 3.34: Indication of equal positive and negative capacitances calculated from phase measurements.

The two element circuit used to represent the growing film is a simplification but proved useful for direct estimation of the electrical properties of the growing film. The phase element was considered to be an ideal capacitor for calculation purposes.

3.4.2 Electrical Properties and the Flow Instability Hypothesis

3.4.2.1 Resistance

The resistance is a measure of the material opposing the passage of ionic current through the uniform oxide layer and the barrier layer once pores develop. To be consistent with a flow instability and dynamic re-stabilization model, the resistance must increase during uniform growth, indicate an onset of structure development and become stable during steady growth. Generally the behavior of the resistance versus time or charge is consistent with this model. In tandem with the capacitance measurements this confirms the localization of the current in the pore base once structure develops. Furthermore, it is expected that the resistance decreases with current density. The premise is that at higher current density a more substantial space charge maintains a thinner barrier layer despite a greater rate of volume generation. Figures 3.35 and 3.36 show the resistances at the peak potentials. The peak potential corresponds to the moment instability leads to development of the pores, immediately before the material that becomes the pore base is pulled towards the metal interface. Figures 3.37 and 3.38 demonstrate that the resistance after 10 C of charge was passed across each square centimeter of the metal interface decreases with current density at both bulk electrolyte temperatures. For all current densities the steady stage resistance was higher at 0 °C. Two possible reasons are a temperature effect on the oxide viscosity and a decrease in the molar volume of oxide produced at low temperature. From all of the plots of peak resistance against current density it can be observed that at 35 $mA \cdot cm^{-2}$ the material composition has a much smaller effect on resistance than at 5 $mA \cdot cm^{-2}$. This separation in resistances for the different materials decreases in the steady stage measure of resistance.

Alloying element incorporation in the growing film may be increasing the resistance in several ways. The elements may be decreasing the viscosity of the oxide as "contaminants" in the oxide lattice have been shown to do. Furthermore, cation ejection occurs during porous growth, but to date no study suggests that aluminum ions must be ejected. Cations with higher mobility in the oxide layer are ejected and the formation of aluminum oxide from oxidized aluminum is more efficient. The percentage of ionic current carried by cations may also be influenced by material composition

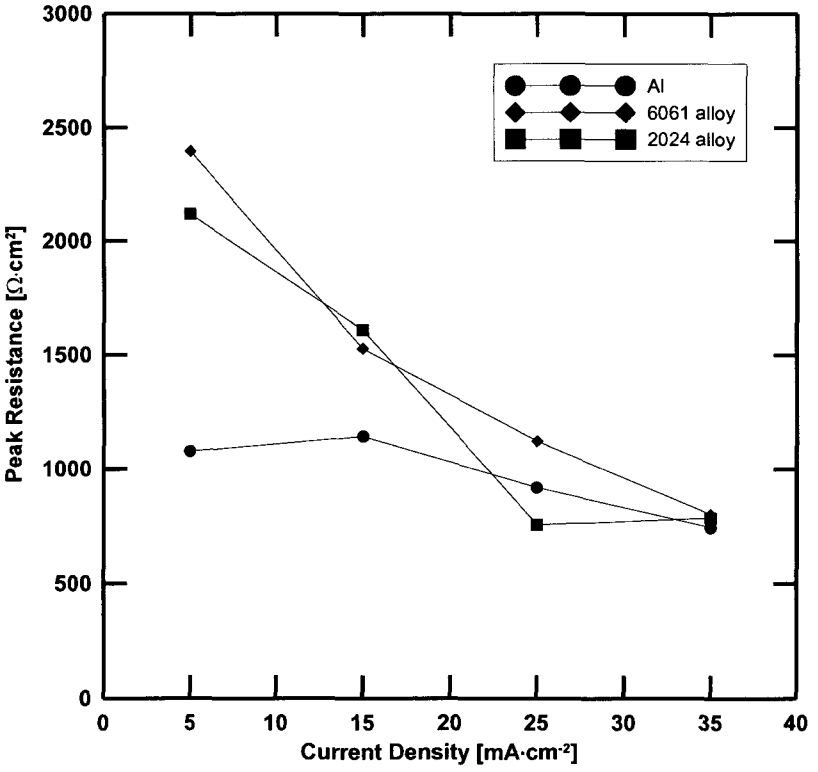

Figure 3.35: Peak resistance against current density at 0°C.

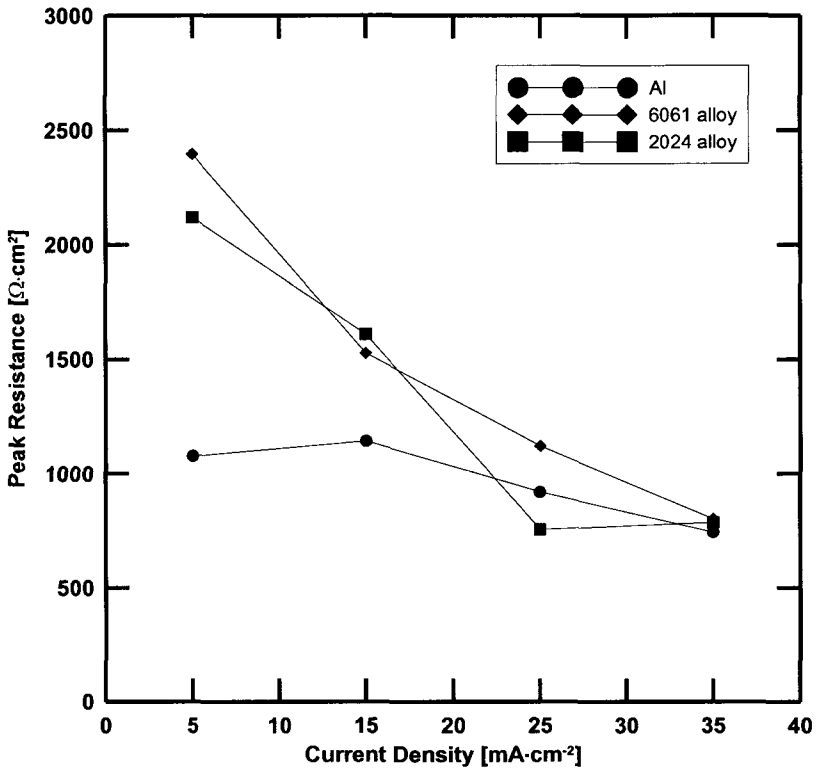

Figure 3.36: Peak resistance against current density at 20°C.

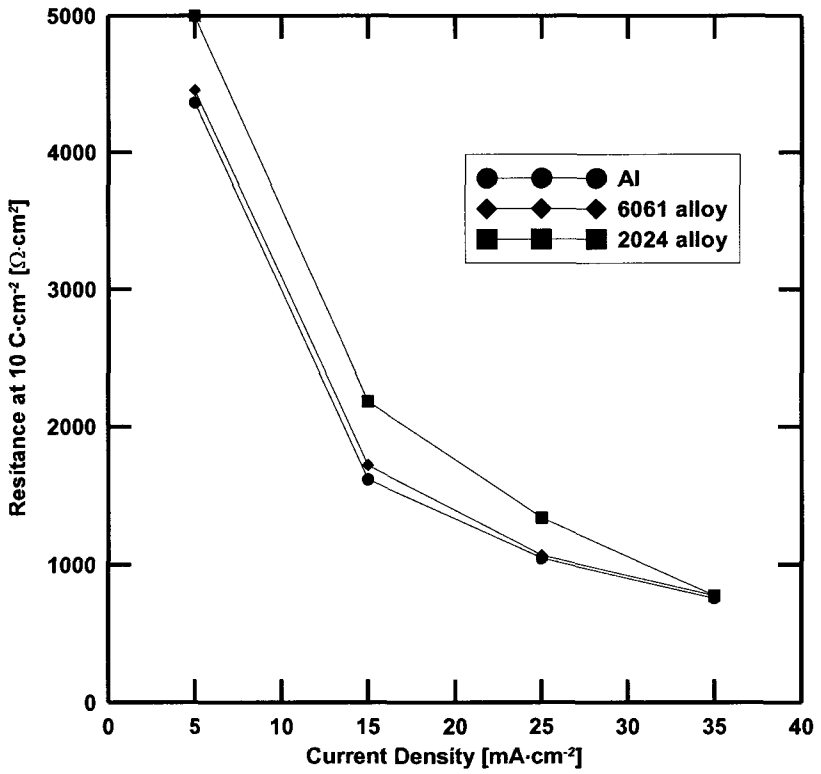

Figure 3.37: Steady stage resistance against current density for films formed at 0°C.

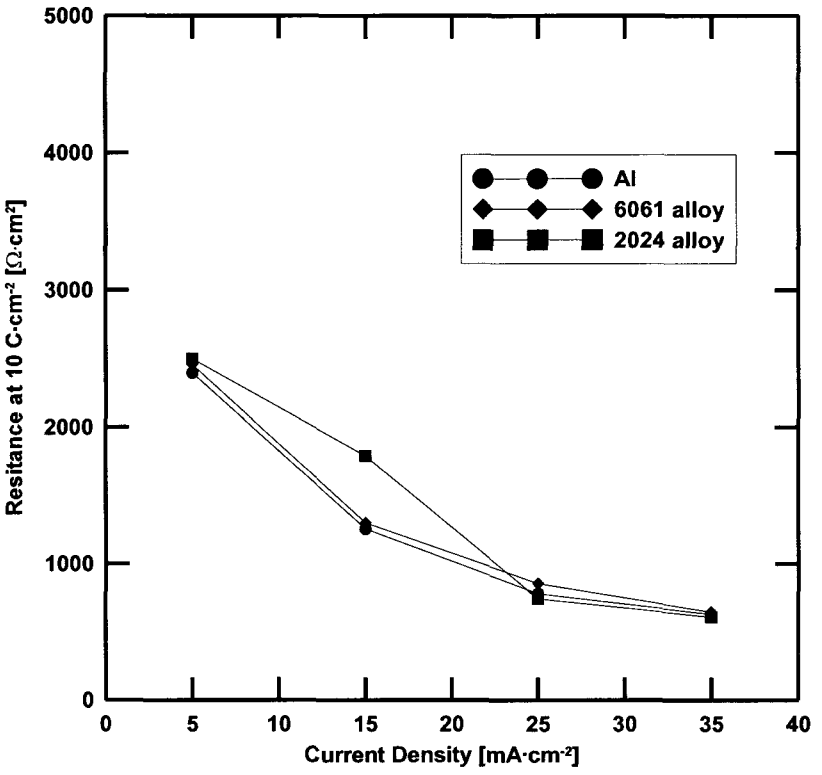

Figure 3.38: Steady stage resistance against current density for films formed at 20°C.

Several cases exist where the resistance indicates the film developed through two stages of instability. Figure 3.4 shows this behavior for pure Al at 15 $mA \cdot cm^{-2}$. It also appears in multiple cases of 2024 alloys, thus seemingly indicating the metal composition's effect on instability. It is hypothesized that as rapid uniform growth becomes unstable and begins to order, the pore ordering and arrangement does not project the pores to the final barrier layer thickness, but instead the barrier layer continues to thicken. The porous structure concentrates the current density and causes a second rapid increase in the oxide thickness; the secondary instability develops and results in the final porous structure. In alloy anodizing elements other than aluminum are oxidized and may or may not form oxide material. The stages of growth apparent in 2024 anodizing could be accounted for by ejection of alloying element ions, thus the rate of aluminum oxide

formation is comparatively slow. Once high mobility alloying elements have been oxidized and ejected, growth proceeds more similarly to pure aluminum anodizing.

3.4.2.2 Capacitance

The capacitance of a growing film is an indication of the dielectric material separating oppositely charged interfaces. At the frequency chosen the capacitance is taken to be that of the uniform oxide before pore development and that of the barrier layer once porous structure develops. To be consistent with an electrostatic induced instability model, the capacitance must decrease during uniform growth as the interfaces move away from each other. When the instability develops, the capacitance should rapidly increase as the space charge concentrates in the pore base and is attracted to the metal interface. Re-stabilization through viscous dissipation would be demonstrated by a steady capacitance as the barrier layer remains a constant thickness. Fluctuation in the capacitance is expected as the charged interface is a region, not a discrete plane. Generally the capacitance behavior is consistent with the flow instability and dynamic re-stabilization hypothesis. Figures 3.39 and 3.40 demonstrate the effect of current density on capacitance. At high current density oxide is formed rapidly. Assuming all oxidized metal reacts with oxygen, the increase in thickness of a uniform film would be 16 $nm\text{-}s^{-1}$; for comparison at 5 $mA\cdot cm^{-2}$, the rate of increase is 2.3 $nm\cdot s^{-1}$. However, the formation of oxide is not 100 % efficient. If an efficiency of 50 % is assumed over the range of current densities, then the injection of Al^{3+} from the oxide is at a rate of 6 x 10^{-8} $mol\cdot s^{-1}$ and 9 x 10^{-9} $mol\cdot s^{-1}$ for 35 and 5 $mA\cdot cm^{-2}$ respectively.

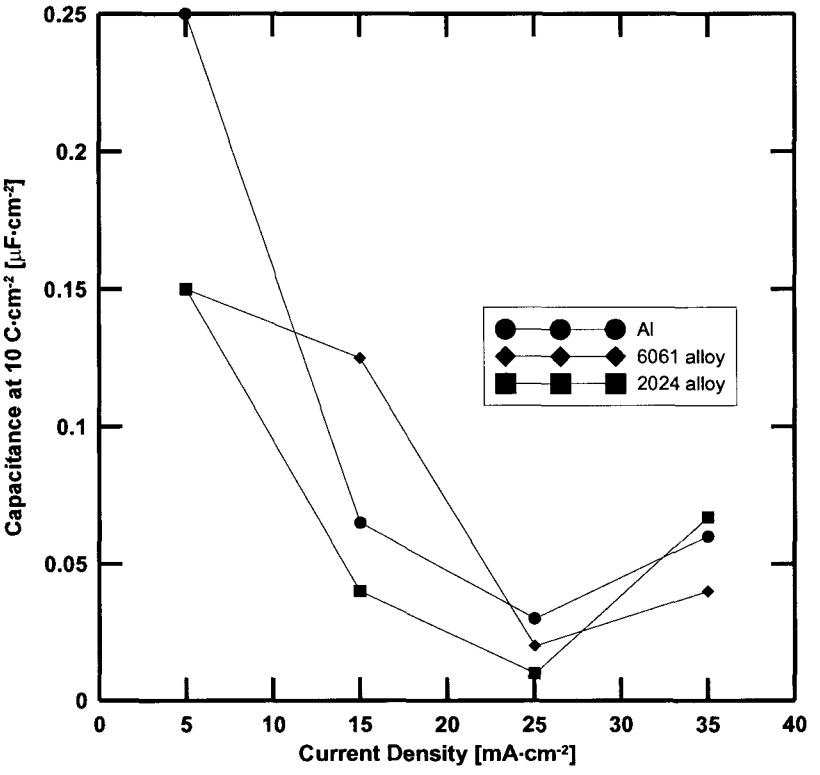

Figure 3.39: Steady stage capacitance against current density at 0°C.

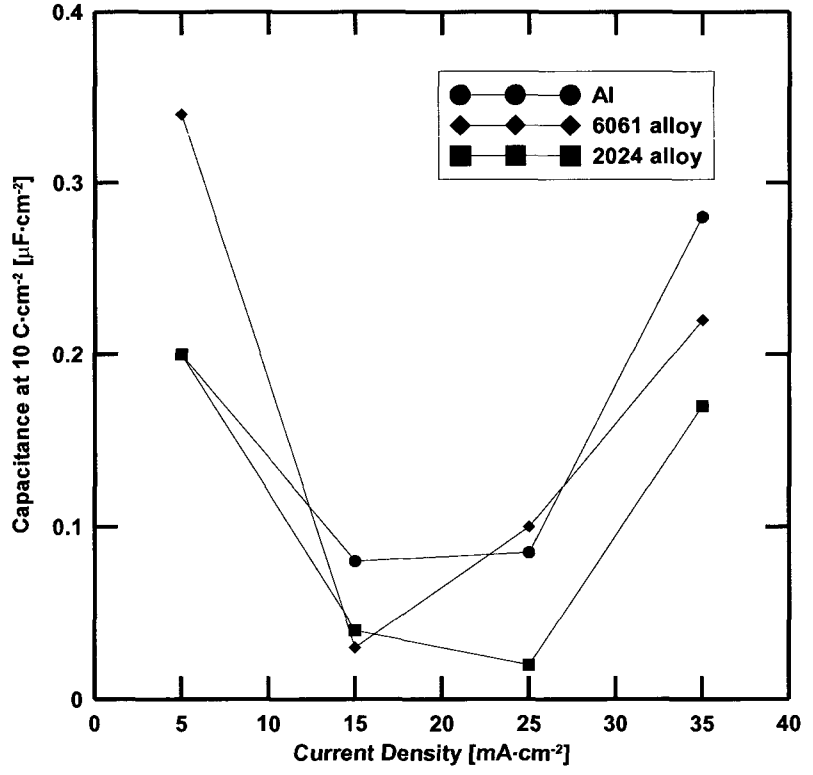

Figure 3.40: Steady stage capacitance against current density at 20°C.

The ejection of positively charged metal cations into the electrolyte at the pore base is thought to have a significant impact on the measurement of the capacitance, the electrostriction stress and the pore dimensions. Initially, when the porous layer is relatively thin, metal cations are removed from the solution filling the pore. The pore diameter, spacing and barrier layer thickness are adjusted by the attraction between interfaces and the repulsion both of charges at the pore base and between adjacent pores. Once the porous film thickens and metal cations concentrate in the pore base the pore diameter and spacing re-adjust to a diminished repulsive force. The barrier layer also tends to thicken by the same neutralizing effect of metal cation ejection.

Furthermore the capacitance or the field across the film can be used to estimate the contribution of electrostriction. Figures 3.41, 3.42, 3.43 and 3.44 display the electrostriction pressure. In each case the calculated electrostriction is on the order of MPa over the geometric area of the electrode. When considered over the area occupied by pores the contribution of electrostriction is more significant. Furthermore, if the contribution of electrostriction is assumed to be at the center of the pore base decaying to negligible at the cell boundary, a pressure gradient between the pore center and the cell boundary is substantial enough to drive the flow of oxide. This is addressed in more detail in the following section.

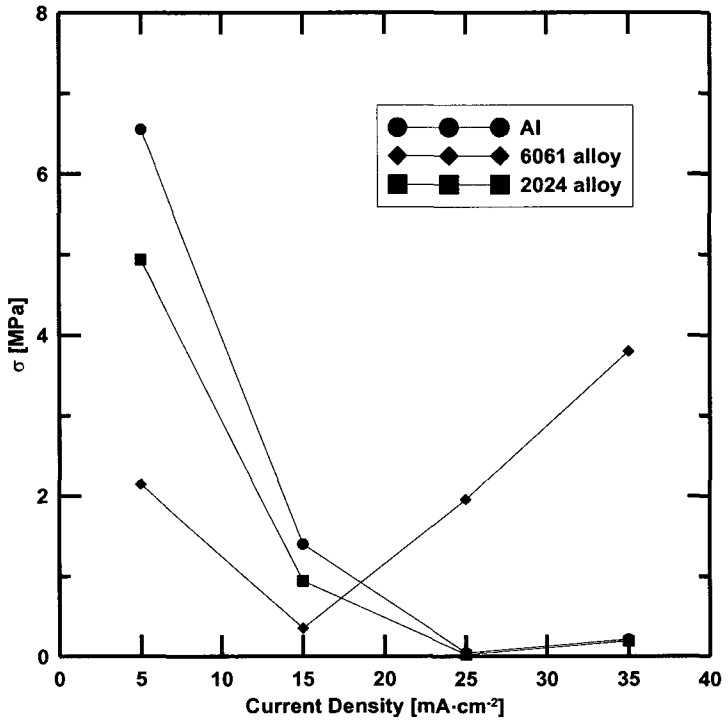

Figure 3.41: Peak electrostriction contribution from capacitance, plotted against current density at 0°C.

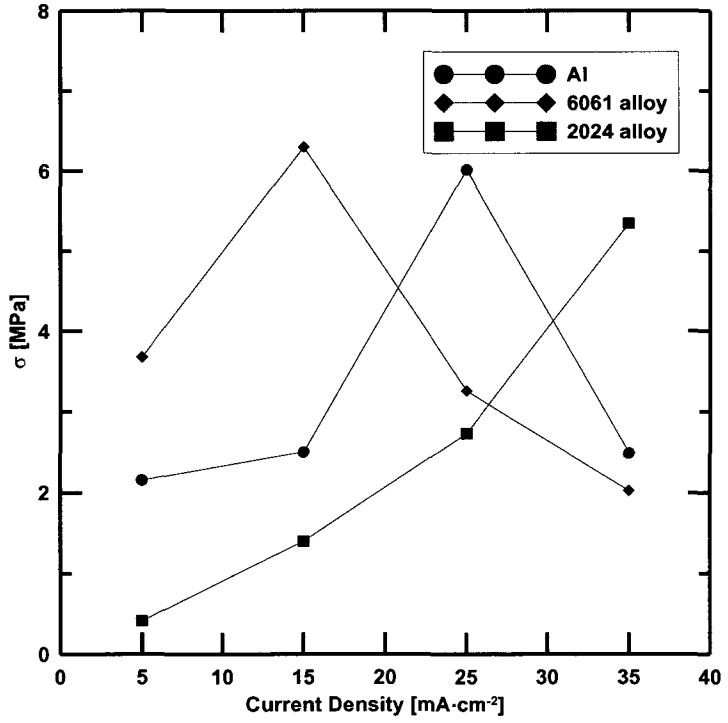

Figure 3.42: Peak electrostriction contribution from faradaic thickness, plotted against current density at 0°C.

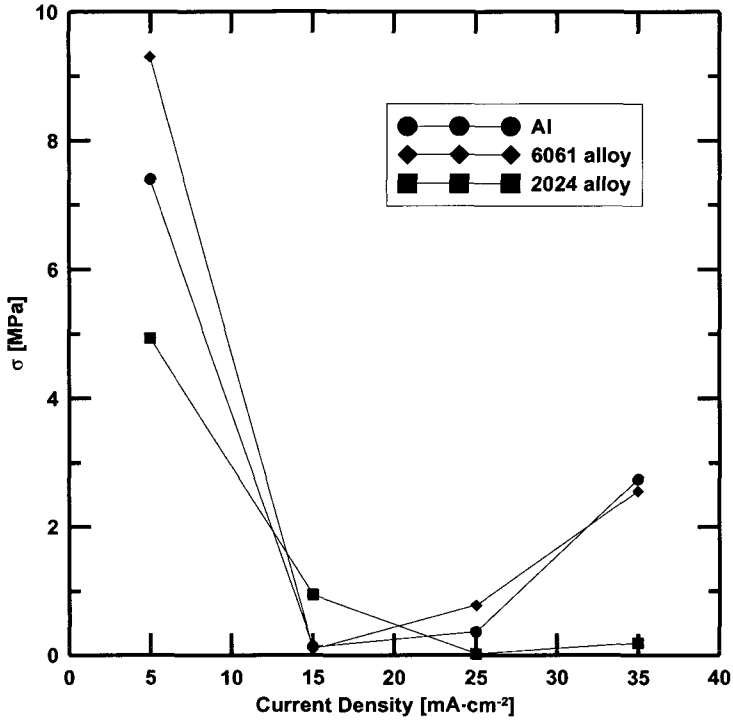

Figure 3.43: Peak electrostriction contribution from capacitance, plotted against current density at 20°C.

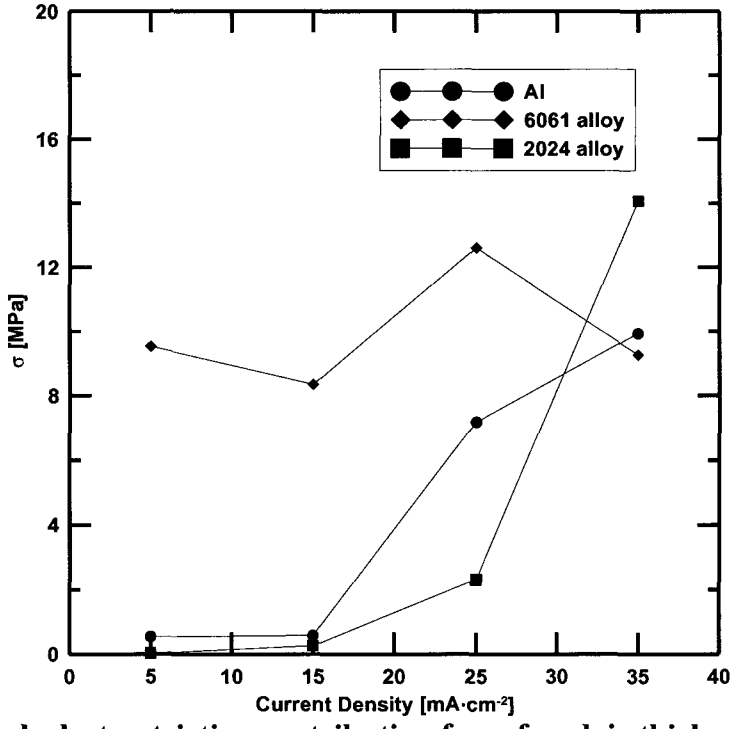

Figure 3.44: Peak electrostriction contribution from faradaic thickness, plotted against current density at 20°C.

3.4.3 Electrostriction at Peak Potential

An electrostriction pressure exists between the two oppositely charged interfaces, its magnitude capable of causing breakdown or deformation of the film[23,27]. The metal interface is fixed, thus the oxide/electrolyte interface is the site of deformation. The electrostriction stress can estimated using the coulombic attraction for a flat metal surface as presented by Vanhumbeeck and Proost.[27]

$$\sigma = -\frac{\nu}{1-\nu}\frac{\varepsilon\varepsilon_o}{2}E^2 \qquad (3.4)$$

The ν is the Poisson coefficient of the film, 0.21 for aluminum oxide, and the electric field E can be estimated by the potential drop, ΔΦ, across the barrier layer thickness, d. The relative permittivity, ε, of alumina is taken to be 10, and the permittivity of free space, ε_0, is 8.85 x 10^{-12} $F \cdot m^{-1}$.

$$E = \frac{\Delta\Phi}{d} \qquad (3.5)$$

At the peak potential the oxide layer is at the maximum thickness. Any non-uniform thinning of the oxide results in a region of increased electrostriction force. Since the viscosity of the film is on the order of 10^9 $Pa \cdot s$[28,29], the electrostriction force must be large enough to cause the oxide to flow outward from the pore base as it approaches the metal. The outward flowing material becomes the pore wall, and boundaries where flow is confined by a developing adjacent pore become the cell limits. Figures 3.41, 3.42, 3.43, and 3.44 show the electrostriction stress in MPa over the geometric surface, more than enough stress to cause flow on the scale of local thinning leading to pore development. Estimation of experimental electrostriction relies on a realistic calculation of thickness from the capacitance data. Some thicknesses were determined to be on the order of μm in

the first seconds of growth, which falls outside the maximum possible thickness. The maximum thickness of a film is that calculated using the faradaic current and 100 % oxide formation efficiency. Figures 3.41-42 and 3.42-43 display the electrostriction pressure in pairs calculated from the capacitance measurement and faradaic thickness respectively. When the same pressure is distributed over the area of the pore base and the pressure gradient is calculated assuming the contribution of electrostriction decays at the cell boundary, the gradient is on the order of 10^{14} Pa-m. The contribution of electrostriction at the pore base is significant enough to be the sole origin of mechanical energy driving flow.

3.4.4 Effect of Sample Composition

Three materials were subjected to the anodizing conditions explained in chapter 2. The behavior of pure aluminum is taken to be a baseline for comparison of two aluminum alloys. When alloys are anodized, the alloying elements play a key role. The alloy compositions are included in table 3.1. For the purpose of this study a major element of interest is copper. Copper has a greater mobility than aluminum in the barrier layer. This means that copper is oxidized by the anodic current, migrates across the barrier layer and enters solution more easily than other alloying elements. Some amount of copper also reacts to form copper oxide or form copper nano-particles[30]. In the case of 2024 alloy, where the copper is around 5 % by mass, there was an abundant supply of copper ion ejected into solution, as indicated by copper reduced at the counter electrode. Accordingly, the faradaic growth on alloys is inefficient; meaning the amount of oxidized metal that forms the oxide film is less than pure metals.

In the figures presenting the resistance as a function of charge passed the resistance for a high copper alloy peaks after more charge is passed, but also progresses through multiple transient phases. Two cases are presented where behavior of the alloy samples are inconsistent. In the related figures 3.35 and 3.36 2024 alloy anodized at 25 $mA \cdot cm^{-2}$ in 20 °C did not follow the expected trends for peak potential and resistance. At the working electrode copper enters the electrolyte at the pore base. Metal cations in solution may reduce the attractive force between the pore base and the metal interface by reducing the effective negative charge or shielding two opposing charges. The behavior also has an immediate impact on barrier layer thickness. Electrostriction pulls the two interfaces together to determine the barrier layer thickness. Accumulation of metal ion in the pore base again effectively reduces that attractive force and volume production at the metal oxide interface forces the pore base away from the metal. Diffusion along the pore to the bulk electrolyte is the only way to remove positive metal and hydrogen ions when films are thick. During the early stage of film growth, agitation may provide some convective movement of fluid, although not on the scale of the pore diameter. Patermarakis estimated the inward motion of water and outward motion of metal cations by considering linear concentration profiles[31]. Without the field the time for ion transfer can be estimated with a diffusivity and pore length. An observed effect of charge shielding would be reduction of both pore diameter and cell separation. Assuming anions collect in a thinning region of film to form a pore, the diameter and spacing are governed by the repulsive force between like charges. If the region experiences charge neutralization due to metal cations ejected from the oxide, then the pore diameter will decrease and the cell separation will also decrease. Films are observed to possess this

structure, and exhibit a wider pore opening at the film surface, described as a trumpet shape. This has been attributed to dissolution of the pore walls[32].

3.4.5 Electrolyte Temperature and Electrical Properties

Electrode and electrolyte temperatures have significant impact on the final structure of porous AAO films[33]. Aerts et al. demonstrate that by using a novel electrode holder both temperatures can be controlled independently and further show that during galvanostatic anodizing the forming potential is more sensitive to the electrode temperature. In this study only the electrolyte temperature was controlled. Two industrially significant temperatures were chosen and agitation was used to minimize the temperature gradient. However, the experimental apparatus does not include an indication of the electrode temperature directly. As such, there is assumed to be some heating of the film as current is passed across the barrier layer. It is well documented that film growth at low temperature results in thicker barrier layers and larger cell dimensions. The electrical properties presented in this study indicate agreement with temperature variability of porous films. The peak potentials are generally higher and increasing with current density at 0 °C and, the corresponding peak resistances are higher and decrease with current density at 0 °C. The resistance is an indication of the barrier layer thickness. Thus, at low temperature the barrier layer is thicker at each current density for each material. During steady stage growth the resistance at high current density is less sensitive to electrolyte temperature. Figures 3.37 and 3.38 indicate that at 25 and 35 $mA \cdot cm^{-2}$, regardless of temperature, the resistance is approximately 1 $k\Omega \cdot cm^2$. At higher current densities the electrolyte temperature may fail as an appropriate indication of the electrode temperature. The barrier layer is subject to some heating as current passes through the layer. At 35

$mA \cdot cm^{-2}$, for every material and at each temperature the final resistance is consistent. Alternatively, the capacitance data is an indication of the barrier layer behavior. The steady growth capacitance indicates a lower capacitance at 35 $mA\text{-}cm^{-2}$ for those films formed at 0 °C. The capacitance is inversely proportional to charge separation, indicating the barrier layer is thicker at low temperature.

3.4.6 Recognizing Instability

Barkey and McHugh presented stability criteria derived using linear stability analysis of an initially uniform oxide film[2]. They assume the flowing oxide to be Newtonian and the motion to be thin creeping flow and demonstrate that an electrostatically compressed film is unstable to long waves

$$\alpha = \alpha_o \exp\left[(2\pi)^2 \frac{4d_o^3}{3\mu}\left(2\frac{(\Delta\Phi)^2 \cdot \varepsilon\varepsilon_o}{\lambda^2 d_o^3} - \frac{4\pi^2\gamma}{\lambda^4}\right)t\right] \tag{3.6}$$

where α is the amplitude of a periodic perturbation, λ is the wavelength, physically represented by the pore spacing, γ is the surface excess free energy of the oxide, μ is the viscosity, taken to be on the order of 10^9 Pa-s, and d_o is the oxide thickness, assumed to be constant because the growth rate is small compared to the time scale of the instability. The relative permittivity, ε, of alumina is taken to be 8, and the permittivity of free space, ε_0, is 8.85×10^{-12} $F \cdot m^{-1}$. When the exponent in equation 3.6 is positive the film is unstable. They include a calculation of the fastest growing special period using the pore spacing, diameter, and barrier layer thickness correlations of O'Sullivan and Wood for AAO film production in phosphoric acid[12]. The scale analysis based on equation 3.6 predicts a diameter to barrier layer thickness ratio of 0.2, an order of magnitude smaller than that measured by O'Sullivan and Wood.

The *in situ* collection of electrical properties introduces several possibilities for the calculation of film thickness on the onset of pore development and an investigation of equation 3.6. Film thickness can be calculated using the capacitance and parallel plate approximation; estimated using the calculated resistance and oxide conductivity; and using the faradaic current.

Analysis of the time constant of equation was undertaken for each temperature, material and current density. The time constant was calculated with thicknesses estimated from the capacitance, faradaic current with 100 % oxide formation efficiency and an oxide conductivity on the order of 10^{14} $\Omega \cdot m^{-1}$. For films that were not analyzed using SEM the pore spacing was estimated using the O'Sullivan and Wood correlation, 2.77 $nm \cdot V^{-1}$. This puts pore spacing on the range of 10-80 nm, consistent with those films that were SEM analyzed films. Generally, the calculated time constants indicated that the films were stable at the potential and resistance peaks. This may be due to an underestimation of the pore spacing.

Barkey and McHugh show the film is unstable when the time constant of equation 3.6 is positive. For that criterion to be met the following condition applies

$$2\frac{(\Delta\Phi)^2 \cdot \varepsilon\varepsilon_o}{\lambda^2 d_o^3} > \frac{4\pi^2\gamma}{\lambda^4} \tag{3.7}$$

Or

$$\frac{\lambda^2}{d_o^3} > \frac{2\pi^2\gamma}{(\Delta\Phi)^2 \cdot \varepsilon\varepsilon_o} \tag{3.8}$$

meaning, the film is unstable for long waves or larger pore spacing. Experimentally, the steady growth cell spacing is frequently on the same order as the barrier layer thickness. O'Sullivan and Wood reported 2.77 and 1.04 $nm \cdot V^{-1}$ for the spacing and barrier layer

thickness respectively[12]. These correlations were derived from measurement of films that had entered the steady growth stage and therefore, give little insight into the onset of porous structure.

Alternatively, the time constant of equation 3.6 and experimental values can be used to predict the pore spacing. In a scale analysis the faradaic thickness is taken to be reasonable to the point of instability as the film is growing uniformly. For a specific case of porous film growth at 5 mA-cm^{-2} and 0 °C, the formation potential and resistance of pure aluminum peaked at 52 s. The thickness from capacitance measurements was 27 nm and the faradaic current thickness was 50 nm. Again, the thickness was based on 100 % efficiency while 27 nm indicates an efficiency of 54 %, which is within range of other study values. The peak potential in this case was 20 V. Taking a permittivity of 10 and a surface excess free energy of 0.1 J·m^{-2} the film is unstable when

$$\lambda = \sqrt{22.3nm^{-1} \cdot d_o^3} \tag{3.9}$$

Using each of the thicknesses indicated above, equation 3.9 gives a range of 25-33 nm for the wavelength of the instability with the lower bound being obtained directly from the capacitance calculation. The O'Sullivan et al. correlation gives a cell spacing of 55 nm at the peak potential. In this case the steady growth stage potential is also 20 V so the final pore spacing based on the correlation is the same. The comparison of the pore spacing indicates that pores initially develop in close proximity and adjust through the transient stage while the cell boundaries are redefined by material flow and charge repulsion. The proximity of the predicted wavelength leading to porous growth and an experimental correlation of the pore spacing is no doubt promising evidence that the electrostriction

induced flow instability proposed by Barkey and McHugh be further scrutinized as the origin of porous AAO growth.

The discussion above began with indicating the electrical properties collected *in situ* during porous film growth describe the concentration of the current, space charge, and electric field in the pore base once structure develops. This observed behavior is consistent with a mechanical deformation and flow origin of the ordered nano-structure in porous anodic aluminum oxide films. Collection of the resistance and capacitance data also lead to calculation of the contribution of an electrostriction force. This contribution is capable of supplying the mechanical energy required to cause flow of newly formed oxide in the barrier layer. The discussion of electrical property behavior was extended to materials other than pure aluminum at multiple current densities and temperatures.

CHAPTER 4

CONCLUSIONS AND RECOMMENDATIONS

4.1 Conclusions

Two electrical properties contain important information regarding the driving forces behind structure development in nano-porous alumina films. The resistance and capacitance indicate the distribution of the current, space charge and electric field. Calculation of the electrical properties was accomplished using an existing non-destructive *in situ* technique. For the first time this technique was used to simultaneously form an ordered porous oxide and extract the desired electrical properties. The time evolution of the resistance and capacitance, when coupled with the structure development, support a flow instability and dynamic re-stabilization hypothesis.

This work contains the application of an existing technique that contributes greatly to the field of nano-porous oxide growth. A model that fully describes the multiple phases of growth observed in porous film production will unlock the incredible functionality of these nano-materials. Considering the present breadth of applications for the relatively narrow range of commercially available alumina films, it is inconceivable that interest in ordered nano-materials will diminish. To fully exploit the incredible functionality of these materials a model must be developed that predicts the film dimensions based on cell conditions. Critical to this success is the type of understanding of driving forces evident in this work.

4.2 Recommendations

Although significant development of this *in situ* single frequency EIS technique has been undertaken it has been recognized as a necessity to investigate the effect of A.C. amplitude and frequency on film growth and properties. Extending analysis using the *in situ* technique to lower and higher current densities will help indicate whether a transition in pore origin exists. The technique may also be applied to an electrochemical system for producing non-porous oxide films. This investigation would indicate the contribution of electrostriction resulting from charges spanning the oxide/electrolyte and metal/oxide interfaces. Furthermore, intensive studies throughout the transient growth stage would benefit from SEM analysis. Using observed film dimensions will help explain the electrical property behavior and stability of the films.

APPENDIX

A.1 Sample Calculations

In section 1.5 the theory behind the circuit model simplification and calculation of two electrical properties was presented. The following is an elaboration using data collected *in situ* using the single frequency technique. The Virtual Instrument (VI) used for data logging outputs two files. One file contains raw data, that is, the direct measurement of current and potential with respect to time over a sample interval long enough to capture 10 cycles. An example of that raw data was presented graphically in figure 3.1. The second output is a summary of the raw data. This output file contains the important attributes of the current and potential signals as calculated using algorithms developed by National Instruments. Tables A.1 and A.2 are examples of the summary files maintained for each material at each current density and temperature. The tables appear disjoined because of space constraints.

These summary tables contain all the data necessary for calculation of each electrical property. The resistance was calculated using the D.C. offset of each channel, Ohm's Law and a scaling adjustment. For example, using the above data at an adjusted time of 5 seconds the D.C. current was -0.127 meaning -12.7 mA, and the D.C. potential was 0.444, meaning 4.44 V. The resistance calculated for this measurement using equation 1.9 and the geometric surface area is 875 $\Omega \cdot cm^2$. The calculation of the capacitance requires analysis of the columns titled "shift." The National Instrument algorithm for phase measurement identifies the frequency of the most prominent signal and measures the phase shift by comparing it with a standard reference wave. In tables A.1 and A.2 it can be seen that at an adjusted time of 5 s, the shift of the current and

potential signals was 45.279° and 191.433° respectively. However, shifts greater than 180° or less than -180° need to be unwrapped, the unwrapped shift of the potential signal is 11.433° and the current signal leads the potential signal by 33.9°. Equation 1.13 can be used to calculate the resistance of the film to the probing A.C. signal. The amplitude of the A.C. signal is small with respect to the D.C. bias. The amplitude of each signal can be found by taking the absolute difference between the positive or negative peak and the D.C. offset. Continuing the example above, the amplitude of the potential signal over the 10 cycles collected for the sampling interval after 5 seconds of growth was 0.003 or 0.03 V. The amplitude of the current signal was 0.011 or 1.1 mA. The raw values reflect the scaling of the DAQ. The calculated resistance to the A.C. probing signal is 33 Ω and the capacitance calculated using equation 1.14 is 0.64 $\mu F \cdot cm^{-2}$.

Table A.1: Summary for the current channel including adjusted time (adj), raw time, D.C. offset (DC), root mean squared value (RMS), positive peak (+peak), negative peak (-peak), detected frequency (det freq.), and phase shift (shift [deg]).

		CURRENT					
adj time	raw time	DC	RMS	+peak	-peak	det freq.	shift [deg]
0.000	4.500	-0.127	0.127	-0.116	-0.137	1999.939	38.567
0.500	5.000	-0.127	0.127	-0.116	-0.137	1999.990	-135.851
1.000	5.500	-0.127	0.127	-0.116	-0.137	2000.078	36.262
1.500	6.000	-0.127	0.127	-0.116	-0.138	2000.010	-55.320
2.000	6.500	-0.127	0.127	-0.116	-0.137	2000.076	-56.091
2.500	7.000	-0.127	0.127	-0.116	-0.138	2000.082	215.891
3.000	7.500	-0.127	0.127	-0.116	-0.137	1999.980	46.523
3.500	8.000	-0.127	0.127	-0.116	-0.137	2000.052	-55.709
4.000	8.500	-0.127	0.127	-0.116	-0.137	2000.031	223.988
4.500	9.001	-0.127	0.127	-0.116	-0.138	2000.120	135.493
5.000	9.501	-0.127	0.127	-0.116	-0.138	2000.047	45.279

Table A.2: Summary for the current channel including D.C. offset (DC), root mean squared value (RMS), positive peak (+peak), negative peak (-peak), detected frequency (det freq.), and phase shift (shift [deg]).

VOLTAGE					
DC	RMS	+peak	-peak	det freq.	shift
0.099	0.099	0.101	0.095	2000.319	198.843
0.137	0.137	0.139	0.134	1997.359	29.056
0.175	0.175	0.177	0.172	2000.693	188.499
0.212	0.212	0.215	0.209	2000.750	97.938
0.248	0.248	0.250	0.245	2000.888	95.572
0.280	0.280	0.282	0.277	2001.574	3.891
0.313	0.313	0.316	0.310	2001.230	195.907
0.345	0.345	0.348	0.342	2000.743	94.358
0.378	0.378	0.382	0.375	1999.131	14.654
0.411	0.411	0.414	0.408	2001.123	-76.885
0.444	0.444	0.447	0.441	2001.510	191.433

NOMENCLATURE

C	capacitance
CPE	constant phase element
d	uniform film thickness, charge separation and barrier layer thickness
D	pore diameter
I_{AC}	alternating current
I_{DC}	direct current offset
I_m	amplitude of the alternating current
R_{bl}	barrier layer resistance
R_p	pore wall resistance
R_s	solution resistance
t	time

V_{AC}	alternating potential analogous to alternating current
V_{DC}	offset potential analogous to direct current
V_m	amplitude of the periodic potential
Z	impedance

GREEK SYMBOLS

α	amplitude of a periodic perturbation
γ	surface excess free energy
ε	permittivity of free space
ε_o	permittivity of alumina, a value of 10 is used
θ	the phase shift in degrees of the periodic current
λ	pore spacing
μ	oxide viscosity
ν	molar volume
σ	the electrostriction stress
ϕ	the phase shift in degrees of the periodic potential
Ω	Ohm, the measure of resistance
ω	radian frequency

WORKS CITED

1. Barkey, D. Transport and Pattern Formation in Anodizing. *18th International Anodizing Conference of the Aluminum Anodizers Council* (2009).

2. Barkey, D. & McHugh, J. Pattern Formation in Anodic Aluminum Oxide Growth by Flow Instability and Dynamic Restabilization. *J. Electrochem. Soc.* **157**, C388 (2010).

3. Zhou, F. et al. Volume Expansion Factor and Growth Efficiency of Anodic Alumina Formed in Sulphuric Acid. *J. Electrochem. Soc.* **158**, C202 (2011).

4. Masuda, H. & Fukuda, K. Ordered Metal Nanohole Arrays Made by a Two-Step Replication of Honeycomb Structures of Anodic Alumina. *Science* **268**, 1466 -1468 (1995).

5. Masuda, H., Hasegwa, F. & Ono, S. Self-Ordering of Cell Arrangement of Anodic Porous Alumina Formed in Sulfuric Acid Solution. *J. Electrochem. Soc.* **144**, L127-L130 (1997).

6. Garcia-Vergara, S.J., Skeldon, P., Thompson, G.E. & Habazaki, H. Stress generated porosity in anodic alumina formed in sulphuric acid electrolyte. *Corrosion Science* **49**, 3772-3782 (2007).

7. Houser, J.E. & Hebert, K.R. The role of viscous flow of oxide in the growth of self-ordered porous anodic alumina films. *Nat Mater* **8**, 415-420 (2009).

8. Baron-Wiechec, A. et al. [sup 18]O Tracer Study of Porous Film Growth on Aluminum in Phosphoric Acid. *J. Electrochem. Soc.* **157**, C399-C407 (2010).

9. Cherki, C. & Siejka, J. Study by Nuclear Microanalysis and O[sup 18] Tracer Techniques of the Oxygen Transport Processes and the Growth Laws for Porous Anodic Oxide Layers on Aluminum. *J. Electrochem. Soc.* **120**, 784-791 (1973).

10. Siejka, J. & Ortega, C. An O[sup 18] Study of Field-Assisted Pore Formation in Compact Anodic Oxide Films on Aluminum. *J. Electrochem. Soc.* **124**, 883-891 (1977).

11. Hoar, T.P. & Mott, N.F. A mechanism for the formation of porous anodic oxide films on aluminium. *Journal of Physics and Chemistry of Solids* **9**, 97-99 (1959).

12. O'Sullivan, J.P. & Wood, G.C. The Morphology and Mechanism of Formation of Porous Anodic Films on Aluminium. *Proceedings of the Royal Society of London. A. Mathematical and Physical Sciences* **317**, 511 -543 (1970).

13. Thompson, G.E., Furneaux, R.C., Wood, G.C., Richardson, J.A. & Goode, J.S. Nucleation and growth of porous anodic films on aluminium. *Nature* **272**, 433-435 (1978).

14. Diggle, J.W., Downie, T.C. & Goulding, C.W. Processes Involved in Reattainment of Steady-State Conditions for the Anodizing of Aluminum Following Formation Voltage Changes. *J. Electrochem. Soc.* **116**, 737-740 (1969).

15. Oh, J. & Thompson, C.V. The role of electric field in pore formation during aluminum anodization. *Electrochimica Acta* **56**, 4044-4051 (2011).

16. Li, A.P., Müller, F., Birner, A., Nielsch, K. & Gösele, U. Hexagonal pore arrays with a 50–420 nm interpore distance formed by self-organization in anodic alumina. *J. Appl. Phys.* **84**, 6023 (1998).

17. Jessensky, O., Müller, F. & Gösele, U. Self-organized formation of hexagonal pore arrays in anodic alumina. *Appl. Phys. Lett.* **72**, 1173 (1998).

18. Su, Z., Hähner, G. & Zhou, W. Investigation of the pore formation in anodic aluminium oxide. *J. Mater. Chem.* **18**, 5787 (2008).

19. Su, Z. & Zhou, W. Porous Anodic Metal Oxides. *Science Foundation in China* **16**, 36-53 (2008).

20. Garcia-Vergara, S.J., Habazaki, H., Skeldon, P. & Thompson, G.E. Tracer studies relating to alloying element behaviour in porous anodic alumina formed in phosphoric acid. *Electrochimica Acta* **55**, 3175-3184 (2010).

21. Skeldon, P., Thompson, G.E., Garcia-Vergara, S.J., Iglesias-Rubianes, L. & Blanco-Pinzon, C.E. A Tracer Study of Porous Anodic Alumina. *Electrochem. Solid-State Lett.* **9**, B47-B51 (2006).

22. Houser, J.E. & Hebert, K.R. Modeling the Potential Distribution in Porous Anodic Alumina Films during Steady-State Growth. *J. Electrochem. Soc.* **153**, B566-B573 (2006).

23. Sato, N. A theory for breakdown of anodic oxide films on metals. *Electrochimica Acta* **16**, 1683-1692 (1971).

24. Van Overmeere, Q., Blaffart, F. & Proost, J. What controls the pore spacing in porous anodic oxides? *Electrochemistry Communications* **12**, 1174-1176 (2010).

25. Zhang, J.-T., Hu, J.-M., Zhang, J.-Q. & Cao, C.-N. Studies of water transport behavior and impedance models of epoxy-coated metals in NaCl solution by EIS. *Progress in Organic Coatings* **51**, 145-151 (2004).

26. Kissell, J.R., Pantelakis, S.G. & Haidemenopoulos, G.N. Aluminum and Aluminum Alloys. 321-463doi:10.1002/0471465186.ch9

27. Vanhumbeeck, J.-F. & Proost, J. On the contribution of electrostriction to charge-induced stresses in anodic oxide films. *Electrochimica Acta* **53**, 6165-6172 (2008).

28. Hebert, K.R. & Houser, J.E. A Model for Coupled Electrical Migration and Stress-Driven Transport in Anodic Oxide Films. *J. Electrochem. Soc.* **156**, C275-C281 (2009).

29. Van Overmeere, Q., Mercier, D. & Proost, J. Experimental Determination of the Viscosity of Anodic Alumina. *ECS Meeting Abstracts* **1101**, 1104 (2011).

30. Curioni, M. et al. Enrichment, incorporation and oxidation of copper during anodising of aluminium–copper alloys. *Surface and Interface Analysis* **42**, 234-240 (2010).

31. Patermarakis, G. Transport phenomena inside the pores involved in the kinetics and mechanism of growth of porous anodic Al2O3 films on aluminium. *Journal of Electroanalytical Chemistry* **404**, 69-76 (1996).

32. Patermarakis, G., Lenas, P., Karavassilis, C. & Papayiannis, G. Kinetics of growth of porous anodic Al2O3 films on A1 metal. *Electrochimica Acta* **36**, 709-725 (1991).

33. Aerts, T., De Graeve, I. & Terryn, H. Anodizing of aluminium under applied electrode temperature: Process evaluation and elimination of burning at high current densities. *Surface and Coatings Technology* **204**, 2754-2760 (2010).